Characterizing Ozone Emissions from Ultraviolet Germicidal Irradiation Air Disinfection Devices: Regulatory Considerations

FINAL REPORT

Hanieh Khoshnevis Ansari
Theresa Pistochini, PhD
Deborah H Bennett, PhD
University of California, Davis

Agreement Number: 24RD017
March 31, 2026

Prepared for the California Air Resources Board and the California Environmental Protection Agency

Disclaimer

The statements and conclusions in this report are those of the authors and not necessarily those of the California Air Resources Board. The mention of commercial products, their source, or their use reported herein is not to be construed as actual or implied endorsement of such products.

Acknowledgment

The authors would like to acknowledge and thank Dr. Wanyu Rengie Chan at Lawrence Berkeley National Laboratory for providing the ozone concentration monitoring data used for calculation of ozone deposition velocity in Appendix B.

This Report was submitted in fulfillment of Agreement 24RD017, *Characterizing Ozone Emissions from Ultraviolet Germicidal Irradiation Air Disinfection*, by University of California, Davis, under the sponsorship of the California Air Resources Board. Work was completed as of March 31, 2026.

Executive Summary

BACKGROUND

Ultraviolet germicidal irradiation at 222 nm (GUV_{222}) has gained significant attention as a whole-room air disinfection technology capable of reducing airborne disease transmission in occupied indoor environments. Unlike traditional 254-nm ultraviolet systems, which must be carefully engineered to prevent direct human exposure, GUV_{222} can be operated in occupied spaces as long as irradiation levels are below thresholds for skin and eye safety. At the same time, the 222-nm wavelength has the capacity to photolyze molecular oxygen, creating the potential for ozone formation indoors. This whitepaper characterizes the ozone-related impacts of GUV_{222}, and compares the resulting ozone levels with those produced by increased outdoor-air ventilation – another method of reducing airborne disease transmission.

OBJECTIVES AND METHODS

Using published irradiance characterizations for GUV_{222} lamps, we developed a spatially resolved irradiance model and applied it to estimate ozone generation for a representative ceiling-mounted GUV_{222} system in an example classroom application designed to be within GUV_{222} eye and skin safety limits. We compared two ceiling heights: 2.45 m and 3.05 m. The resulting ozone generation rate per lamp was 0.88 mg h^{-1} for a ceiling height of 3.05 m and 0.28 mg h^{-1} for a ceiling height of 2.45 m. We then built a mass-balance model for the modeled classroom and compared indoor ozone concentrations for two infection-control strategies: 1) compliance with ASHRAE Standard 241: Control of Infectious Aerosols using outdoor-air ventilation alone, and 2) compliance with ASHRAE Standard 62.1: Ventilation and Acceptable Indoor Air Quality supplemented with three GUV_{222} lamps providing additional clean air through pathogen inactivation. To capture regional variation, simulations were conducted for three California cities – Oakland, Sacramento, and Riverside – representing low, moderate, and high ambient ozone environments.

RESULTS

Across all cities, the GUV_{222} plus ASHRAE 62.1 ventilation scenario yielded lower indoor ozone concentrations than the ASHRAE 241 outdoor-air-only scenario for the classroom application. This occurs because, in most buildings, outdoor air is the dominant source of indoor ozone, and increasing outdoor-air ventilation introduces more ozone indoors than the amount produced by GUV_{222} under realistic irradiance conditions that meet skin and eye safety limits. Based on the modeled conditions, outdoor ozone concentrations would have to average less than 10.7 ppb (3.05 m ceiling) or 6.8 ppb (2.45 m ceiling) for increased outdoor-air ventilation to provide lower indoor ozone exposure than GUV_{222}, thresholds substantially below typical background levels across the U.S. Thus, under the conditions modeled in this paper, GUV_{222} used in conjunction with standard ventilation leads to lower indoor ozone exposure than meeting ASHRAE Standard 241 entirely through increased outdoor-air ventilation.

Although this whitepaper focuses on ozone, the implications for infection control are also important. For the example classroom, we determined that GUV_{222} can deliver equivalent

clean air rates comparable or higher than those associated with increased outdoor-air ventilation, particularly for pathogens with moderate to high UV susceptibility. For air disinfection, the modeled GUV_{222} scenario met or exceeded ASHRAE 241 for pathogen inactivation constants (k_p) greater than 2.3 cm^2 mJ^{-1} for the 3.05 m ceiling scenario and 7.7 cm^2 mJ^{-1} for the 2.45 m ceiling scenario, at a mixing delay of 60 s, with the threshold increasing at longer mixing delays. Because reported k_p values for airborne pathogens vary by an order of magnitude with high uncertainty, and because the air mixing timescale in a given space is similarly difficult to characterize or predict a priori, it is not currently possible to conclude which strategy will dominate for a given pathogen or installation. This uncertainty highlights the critical need for targeted experimental research to better quantify both pathogen-specific susceptibility constants and indoor air mixing characteristics under realistic airborne conditions.

CONCLUSIONS

Collectively, the findings indicate that, when operated within established photobiological safety limits, GUV_{222} can provide infection-risk reduction while maintaining lower indoor ozone levels than high outdoor-air ventilation in most ambient ozone environments. This conclusion, however, applies specifically to ozone; a comprehensive assessment would also consider ozone-reaction byproducts, energy implications of increased outdoor-air ventilation and operation of GUV_{222}, and the performance of filtration-based alternatives, which can provide equivalent clean air without generating ozone. Additionally, the conclusions are limited to the analyzed scenario; additional simulations are needed to draw more general conclusions for a variety of applications. The framework outlined and applied in this paper is a useful tool that can be expanded to consider additional scenarios.

Table of Contents

List of Figures

List of Tables

I. Introduction

I.I History of GUV Technology

The ultraviolet (UV) region of the electromagnetic spectrum spans from 100 to 400 nanometers and is commonly divided into UV-A (315–400 nm), UV-B (280–315 nm), and UV-C (100–280 nm). Within UV-C, scientists often carve out finer subdivisions to reflect differences in photochemical behavior: vacuum UV (<200 nm), far UV-C (roughly 200–230 nm), and the germicidal range, or GUV, spanning 220–280 nm. What sets UV-C apart is its unusually high photon energy, which readily breaks down molecular structures inside living cells. Nucleic acids, in particular, are vulnerable; once DNA and RNA sustain enough damage, replication and transcription grind to a halt, leaving the microorganism unable to survive [1, 2].

For decades, germicidal systems have harnessed this property through low-pressure mercury lamps that emit almost exclusively at 253.7 nm (commonly rounded to 254 nm) [3]. Exposure at this wavelength induces signature DNA damage that disrupts cell division [4]. The catch is that the same radiation that inactivates microbes also damages human tissue. Both skin and eye injuries from 254 nm light are well documented, including erythema (sunburn-like reddening), increased skin cancer risk from DNA damage, and photokeratitis (painful inflammation of the cornea) [5, 6]. As a result, GUV systems built around this wavelength (commonly termed GUV_{254}) must be engineered with strict safeguards to avoid direct human exposure.

GUV_{254} was first deployed in the 1930s, when ceiling-mounted fixtures (with radiation directed toward the ceiling and away from occupants) were designed to cut down on airborne transmission of respiratory diseases [7]. Early adopters were institutions constantly grappling with contagious diseases—schools, hospitals, and clinics—where outbreaks of measles, influenza, polio, and mumps were commonplace [8]. Commercial uptake followed soon after; by 1947, Westinghouse was marketing its "Sterilamp" for routine use in homes and public spaces [9]. Still, the technology never gained real traction. A major hurdle was the medical orthodoxy of the time, which long held that contaminated surfaces, rather than aerosols, were the chief culprits in disease transmission [10]. Only in the 1960s, with tuberculosis (TB) studies pointing squarely to aerosols as a driver of infection [11, 12], did attention focus back on airborne pathways. That shift briefly reinvigorated upper-room GUV_{254} applications, particularly in hospitals, but enthusiasm soon waned as antibiotics and mass vaccination campaigns became the dominant tools of disease control.

The landscape shifted once again in the 1980s and early 1990s, when TB re-emerged on a global scale. Immunocompromised patients were hit especially hard, prompting some healthcare facilities to turn back to GUV_{254} as part of their infection-control strategies. What pushed interest even further was the growing threat of drug-resistant TB and rising fears of airborne bioterrorism [13, 14]. In this period, GUV_{254} interventions were tied to measurable reductions in TB mortality [15], underscoring their potential when properly deployed. These waves of attention—waxing and waning in response to shifting public health priorities and technological advances—are traced in detail in Reed's historical synthesis of GUV's trajectory

[16]. Johnson (2024) tabulated Reed's account into a concise summary, which we reproduce here as Table 1 [17].

Table 1. Key milestones in the history of GUV disinfection (adopted from Johnson (2024))

Year(s)	Milestone
1877	Downes and Blunt discover that sunlight prevents microbial growth, later shown to depend on both dose and wavelength.
1930	Gates publishes the first analytical bactericidal action spectrum, peaking at 265 nm.
1933	Wells introduces the concept of "droplet nuclei" in airborne infection.
1935	Wells and Fair provide experimental proof that GUV systems can efficiently inactivate airborne microorganisms.
1937	Upper-room GUV is introduced in Philadelphia schools to control measles transmission.
1940s-1950s	Attempts to replicate school-based measles control with GUV fail, later attributed to exposures occurring outside school buildings.
1956-1962	Guinea pig studies demonstrate conclusively that TB spreads through the air. Animals breathing air irradiated with GUV remained uninfected, while those exposed to untreated air contracted TB.
1969-1972	Model studies with aerosolized organisms show that effective upper-room GUV requires air mixing, and that efficacy drops under high humidity.
1974-1975	Both TB and Bacillus Calmette–Guérin (BCG) are found to be equally susceptible to UV-C, confirming upper-room GUV's effectiveness for disinfecting the occupied lower room.
1985-1992	The unexpected resurgence of TB in the United States drives renewed interest in GUV for air disinfection.
1990s-present	Research continues on GUV system design, performance, and safety under real-world conditions.

As noted earlier, exposure to 254 nm UV light is well known to damage human skin and eyes, so GUV_{254} systems are restricted to applications that avoid human exposure: running lamps in unoccupied rooms, installing them within HVAC ducts (which has limited contact time between the airborne pathogens and the radiation), or mounting them high enough to restrict exposure to upper-room air [18, 19].

By contrast, studies over the past decade indicate that GUV_{222} may not cause these skin and eye safety concerns below certain exposure limits. Early work suggested that UV-C light at 222 nm can neutralize pathogens without causing measurable harm to mammalian tissue [20-22]. This wavelength is typically produced by krypton–chloride (KrCl*) excimer lamps, which emit a narrow band of radiation centered at 222 nm. However, unfiltered KrCl* lamps also emit small fractions of longer-wavelength UV-C (230–260 nm) that penetrate more deeply into skin and ocular tissue and can induce DNA lesions and erythema. Optical filters are therefore

essential to block these out-of-band emissions and confine the output to the 222 nm region, increasing the safety of these GUV systems when used in occupied environments [23, 24]. If GUV_{222} can be safely applied to continuously irradiate all the indoor air (as opposed to only the upper room), the pathogen inactivation potential of GUV would be increased. In 2018, the Center for Radiological Research at Columbia University demonstrated that ~95% of aerosolized H1N1 was inactivated by a 2.0 mJ cm^{-2} dose of GUV_{222} delivered over ~20 s in their aerosol irradiation chamber, which is equivalent to an inactivation rate constant of 1.8 cm^2 mJ^{-1} [25]. Inactivation rate constants are discussed in more detail in Section II.V.

The arrival of the COVID-19 pandemic brought new urgency to the field. Follow-up studies quickly showed that GUV_{222} was capable of inactivating airborne human coronaviruses as well [26]. Once efficacy had been established, attention turned toward safety. In 2020, Fukui et al. demonstrated that filtered GUV_{222} exposures up to 500 mJ cm^{-2} produced no observable erythema in a cohort of 20 volunteers, with optical filters effectively removing longer-wavelength emissions known to penetrate deeper into tissue [27]. Subsequent work by Eadie and colleagues in 2021 found no acute skin responses (e.g., erythema) even at fluence levels up to 18,000 mJ cm^{-2} under filtered GUV_{222} exposure, though transient skin yellowing was observed at doses of 6,000 mJ cm^{-2} and above [28]. That same year, Hickerson et al. demonstrated that at an applied fluence of 6100 mJ cm^{-2} under filtered GUV_{222} exposure, cyclobutane pyrimidine dimer (CPD) formation remained minimal, was confined to the superficial region immediately beneath the stratum corneum, and was absent in the basal layer where mutagenic risk is highest [29]. Yet the debate is far from settled. Ong et al. found in 2022 that, while GUV_{222} irradiation did not produce the classical UV-induced DNA lesions (cyclobutane pyrimidine dimers or 6-4 photoproducts) or activate apoptotic (cell-death) pathways typically seen after exposure to 254- or 277-nm light, it did cause other signs of molecular stress. Specifically, cells exposed to GUV_{222} showed persistent γH2AX foci, a biomarker of DNA double-strand breaks, and indications of DNA-damage-response. These results suggest that, although 222-nm photons do not induce direct mutagenic lesions characteristic of conventional germicidal wavelengths, they may still trigger secondary stress responses [30]. More recently, work from Eadie's group (2025) has underscored the substantial variability in optical filtering among commercially available GUV_{222} fixtures and how this variability influences their safety profiles. Their findings highlight the need for rigorous spectral characterization and accurate dosimetry to support reliable risk assessment [31]. Nevertheless, the potential long-term molecular consequences of repeated or chronic exposure remain unresolved and are an active focus of ongoing research.

While researchers continue to debate safety, the rollout of GUV_{222} systems in real-world settings is already underway. At the same time, concerns have surfaced over ozone emissions and subsequent ozone-reaction byproducts from GUV_{222} systems. Because photons at 222 nm have sufficient energy to photolyze molecular oxygen ($O_2 \rightarrow 2O(^3P)$), they can initiate ozone formation through subsequent reactions with O_2. Once formed, ozone is highly reactive and can further interact with volatile organic compounds and surface materials indoors, producing a suite of secondary oxidized gases and particles—collectively referred to as ozone-reaction byproducts. For that reason, a comprehensive evaluation of the air quality

impacts of GUV_{222} must consider ozone yields and the negative impact of increased indoor ozone concentration balanced against pathogen inactivation and the positive impact of clean air delivered to the space.

I.II Market Sectors

From a market standpoint, GUV_{222} technology has begun to gain a foothold on both the supply and demand sides. On the supply side, growth has been driven by manufacturers of KrCl* excimer lamps and by firms building integrated systems that combine GUV with optics, filters, and smart controls. Established lighting companies have stepped into the space, while specialized startups and HVAC providers are vying to carve out market share [32]. On the demand side, uptake has been strongest in sectors where infection control is paramount. Healthcare facilities lead the way, deploying GUV_{222} in patient rooms, waiting areas, and surgical theaters. Schools, universities, and office buildings have followed, particularly in the wake of COVID-19, as part of broader investments in indoor air quality. The transportation sector has also shown interest, from airports and subway systems to aircraft cabins, where high passenger turnover makes providing clean air especially difficult. More recently, hospitality and retail venues have begun to explore GUV_{222} as a means of lowering transmission risks while keeping operations running and maintaining public confidence [32].

I.III Regulations on Human Exposure Limits to GUV Radiation

Design and operation of GUV systems in occupied spaces are ultimately bounded by human exposure limits, which are defined in terms of energy density (mJ cm^{-2}) and irradiance (μW cm^{-2}) landing on human surfaces. Two organizations provide guidance on permissible levels: the International Commission on Non-Ionizing Radiation Protection (ICNIRP), which is often invoked through radiation-protection legislation outside the United States, and the American Conference of Governmental Industrial Hygienists (ACGIH) Threshold Limit Values (TLVs), which are the de facto occupational benchmark within the United States. Although both rely on wavelength-dependent hazard weighting, they differ in how limits are expressed and, crucially, in how permissive they are at GUV wavelengths.

ICNIRP sets a single spectrally weighted daily limit for ultraviolet radiation incident on the unprotected eye and on the most sensitive non-pathologic skin types across 180–400 nm, specifying that the effective, spectrally weighted exposure should not exceed 3 mJ cm^{-2}. Application of these limits is mediated by each country's regulatory choices, but in practice the ICNIRP weighting function $S(\lambda)$ governs how much of a given monochromatic exposure counts toward the 3 mJ cm^{-2} daily allowance. At 222 nm, for example, $S(\lambda)$ is approximately 0.134, which means that only about 13% of the incident radiant exposure is counted as "effective." In practical terms, this corresponds to 3 mJ cm^{-2} / 0.134 ≈ 23 mJ cm^{-2} of monochromatic GUV_{222} exposure before the ICNIRP threshold is reached.

The ACGIH TLVs are occupational limits expressed directly as wavelength-dependent daily radiant-exposure values for eye and skin. In 2021, ACGIH updated its UV TLVs, materially increasing allowable daily exposures at the 222 nm wavelength relative to 254 nm,

recognizing reduced risk for the exposure to 222 nm radiation relative to 254 nm radiation [3, 33]. The ACGIH limit for skin exposure is 478.6 mJ cm^{-2} for skin and 160.7 mJ cm^{-2} for eye exposure, substantially higher than the ICNIRP limit (Table 2).

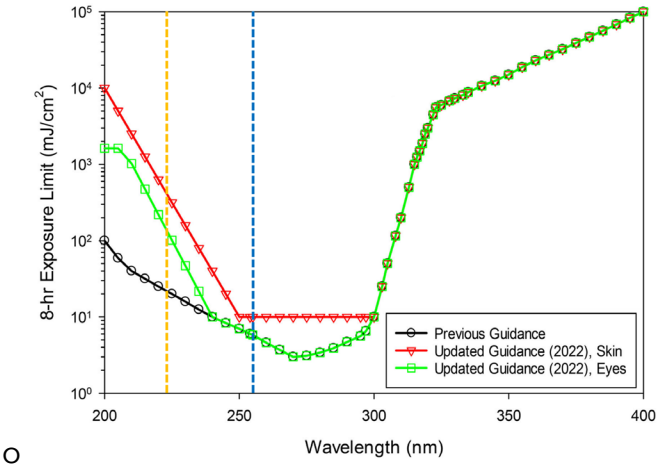

Figure 1. Comparison of ACGIH 8 h TLVs for UV-C radiation. Vertical dashed lines indicate 222 nm (orange) and 254 nm (blue). Adapted from [3].

Table 2. Exposure limits for GUV_{222}, expressed as 8 h cumulative dose and the equivalent constant irradiance.

Limit	**8 h Exposure limit (mJ cm^{-2})**	**Corresponding irradiance (μW cm^{-2}) ***
ICNIRP exposure limit	23	0.8
ACGIH skin TLV (if eyes protected) (2021)	478.6	16.6
ACGIH eye and skin TLV (2021)	160.7	5.6

* estimated from the exposure limit assuming constant fluence rate over 8 h.

The outcome is that ACGIH permits substantially higher daily exposures than ICNIRP for both eye and skin, which can translate to higher allowable lamp outputs, larger treated volumes, or greater design flexibility for whole-room GUV installations. For constant exposure over 8 h, the exposure limit per ICNIRP is 0.8 μW cm^{-2}, whereas the exposure limit per ACGIH is 16.6 μW cm^{-2} for skin and 5.6 μW cm^{-2} for eyes. An important difference is that ICNIRP considers health risks for broad groups of people, whereas ACGIH recommendations are for occupational health and safety.

The Illuminating Engineering Society (IES) standard ANSI/IES RP 27.1-22 Photobiological Hazards from UV Lamps defines the process for measuring the output from UV devices relative to exposure limits and assigning devices to different risk groups [34]. In order to achieve the lowest risk group (RG-0), the standard draws from ACGIH spectral weighting guidance and states that the irradiance from a GUV_{222} device must be less than less than 15.9 μW cm^{-2} when measured 1 m from the source. This value is similar to the ACGIH skin TLV (16.6 μW cm^{-2}), although it is slightly less due to rounding in the calculation. RP 27.1-22 also requires

compliance with ACHIH 8 h exposure limits, although the standard does not specify how to apply time-weighted averages for an occupant moving throughout a room (e.g., higher exposure while standing versus lower exposure while seated).

The International Electrotechnical Commission (IEC) standard IEC/EN 62471: Photobiological Safety of Lamps and Lamp Systems also describes a procedure for assessing UV devices and assigning a risk group for biological safety. However, the IEC relies on stricter spectral weighting guidance from ICNIRP, stating that the irradiance from a GUV_{222} device must be less than 0.75 μW cm^{-2} when measured 1 m from the source to be considered RG-0. IEC/EN 62471 does not have additional requirements for considering the time-weighted average exposure of the person moving throughout the room.

Compliance with UL standard ANSI/UL 8802: Ultraviolet Germicidal Equipment and Systems is required for GUV devices installed and used in the US under the National Electric Code (NEC), which is widely adopted into state and local electrical regulations [35]. ANSI/UL 8802 requires that the device must be classified as RG-0 according to either ANSI/IES RP 27.1-22 or IEC/EN 62471. Because the allowable irradiance limit in ANSI/IES RP 27.1-22 is approximately 6 times higher than that in IEC/EN 62471, manufacturers can meet RG-0 by complying with the less restrictive RP-27.1-22 skin limit of 15.9 μW cm^{-2}, since compliance with either limit is acceptable. There is a general consensus that the higher skin limit is applied for fixtures designed to be installed on ceiling facing down, since only a fraction of the radiation will reach the eyes (which are vertical surfaces shielded from direct radiation by eye lids [36]). ANSI/UL 8802 also specifies that this comparison must be based on the highest measured irradiance (i.e. most severe possible conditions) measured at 1.9 m above the floor at the minimum ceiling height specified for installation by the device manufacturer. This may be closer to the lamp than the distance of 1 m as specified by ANSI/IES RP 27.1-22 and IEC/EN 62471.

In considering these regulations on human exposure limits to GUV radiation for our modeling objectives, we describe and model an example installation and compare its compliance relative to ANSI/UL 8802. Analyzing and applying ANSI/UL 8802 limits is not intended to imply that the authors consider these levels inherently safe for skin or eyes. It is important to recognize that ANSI/UL 8802 limits remain higher than those recommended by ICNIRP, which reflects ongoing differences in expert opinion and regulatory approaches regarding acceptable exposure and safety margins.

I.IV Ozone in Indoor Environments

Ozone is widely regarded as the dominant oxidant indoors. Its concentration inside a building is shaped by several factors: the level of ozone outdoors, the rate at which indoor and outdoor air are exchanged, any indoor sources of ozone, and the rate at which it reacts with surfaces and other airborne chemicals [37]. There are very few sources of ozone generation indoors; other than GUV, sources may include certain electronic devices, ionizers, or photocopiers. When no indoor sources of ozone are present, all ozone indoors results from outdoor air transfer. The indoor-to-outdoor ozone concentration ratio typically falls between 0.2 and 0.7,

depending on air-exchange rates and ozone loss to indoor surfaces [38]. Under typical outdoor conditions, indoor ozone concentration ranges from about 1 to 30 ppb [38].

Ozone removal indoors occurs primarily through surface deposition, where ozone reacts with materials such as carpets, painted walls, furnishings, and human skin [37, 39]. These surface reactions are characterized by deposition velocities that vary widely depending on material type, with higher rates observed on textiles and human occupants compared to hard surfaces [40]. Gas-phase reactions between ozone and volatile organic compounds (such as terpenes from cleaning products, air fresheners, and building materials) also contribute to ozone removal, though typically to a lesser extent than surface deposition [41, 42]. The combined effect of these removal processes results in indoor ozone lifetimes on the order of minutes to tens of minutes, significantly shorter than the multi-hour lifetimes typical of outdoor environments [37, 43, 44].

Chemical reactions within indoor air generally contribute only modestly to the overall ozone balance, but they can produce a variety of oxygenated volatile organic compounds (VOCs) and ultrafine particles, many of which are known to be irritants or otherwise harmful to human health [45]. Common examples of such oxygenated VOCs formed through ozone-initiated reactions include formaldehyde, acetaldehyde, acrolein, and other low-molecular-weight carbonyls, which are associated with respiratory irritation and sensory discomfort. The health implications of these byproducts add to concerns about ozone itself, making it important to minimize both direct ozone exposure and the formation of secondary pollutants.

Controls on indoor ozone emissions enter through both certification and state regulation. UL 867 limits ozone emissions from air cleaners to 50 ppb and is referenced by programs such as ENERGY STAR. UL 2998 provides a voluntary "zero-ozone" environmental claim validation for emissions less than or equal to 5 ppb. Both standards rely on the same test method: the device is placed in a controlled chamber of approximately 27–31 m^3 with an ozone decay rate set to 1.33 h^{-1}, operated continuously for up to 24 hours (an 8-hour test is allowed if concentrations stabilize), and the ozone concentration near the device outlet is monitored throughout. To comply, the measured concentration must remain below the specified limit—50 ppb for UL 867 and 5 ppb for UL 2998. The California Air Resources Board (CARB) requires that indoor air cleaners sold in the state (with some industrial use exemptions) be certified to UL 867 and meet the 50 ppb limit, with packaging labels and a public list of approved models. Importantly, the UL tests report the maximum outlet concentration under test-chamber conditions, which is not equivalent to the ozone increase that would occur in a real building. Shortcomings in current ozone-emission test standards, and ongoing efforts to improve them, are described in Section VII.

I.V Airborne Infection Risk Reduction Standards

Performance expectations for using GUV to reduce airborne infection risk are increasingly structured by consensus guidance. ASHRAE Standard 241 establishes the concept of equivalent clean airflow (ECA) and recognizes GUV (i.e., upper-room, in-duct, or whole-room) as one of several means to meet risk-based targets during periods of elevated concern [46].

Resources from the U.S. Centers for Disease Control and Prevention (CDC) and the National Institute for Occupational Safety and Health (NIOSH) continue to serve as the primary reference documents for upper-room GUV design, commissioning, and maintenance [47, 48]. The Illuminating Engineering Society (IES) *Recommended Practice for GUV Systems* (IES RP-44-21) provides complementary system-level guidance that aligns with photobiological-safety standards such as ANSI/IES RP-27 and IEC 62471-6 [49]. Although adoption remains discretionary, these documents are increasingly shaping how building owners demonstrate due diligence and how engineers document design intent.

I.VI Whitepaper Objectives

The objectives of this whitepaper are to characterize and quantify, using data from existing literature, the relationship between GUV_{222} irradiance, ozone generation and indoor exposure, and associated air-disinfection benefits. In addition, we review relevant ozone-emission test standards applicable to GUV_{222} systems and summarize the potential public-health risks associated with indoor ozone exposure.

To quantify air-disinfection benefits, we follow guidance provided by ASHRAE Standard 241, which prescribes a minimum required ECA based on space type. Standard 241 allows the ECA to be achieved through a combination of dilution by outdoor air (i.e., ventilation), filtration, and air disinfection. Notably, achieving the required ECA solely by increasing outdoor air ventilation may inadvertently elevate indoor ozone concentrations because ozone tends to be higher outdoors than indoors. In typical buildings, there are no significant sources of indoor ozone; therefore, outdoor air is the primary source of indoor ozone. The indoor ozone level increases as the outdoor ozone level increases or outdoor air rate increases. However, the relationship is complex due to the mechanics of ozone deposition and chemical reactions indoors as discussed in Section V.

In a prior whitepaper, we recommended that CARB consider lowering its current ozone emission limit of 50 ppb for air cleaners (as measured by UL 867) to reduce ozone emissions and protect occupant health [50]. A potential reduction to 5 ppb, in line with UL 2998, would decrease allowable emissions by an order of magnitude. However, members of the GUV_{222} industry and research community argue that GUV_{222} devices should be exempt from such potential reductions, citing that their potential for infectious aerosol control may outweigh the public health risks of additional ozone exposure, especially in densely occupied environments. They also contend that increasing outdoor air ventilation (which is not regulated) to achieve the same level of infectious aerosol control could result in greater indoor ozone levels than would occur with GUV_{222} use. In this whitepaper, we seek to answer this important question: how does indoor ozone exposure compare when infectious aerosol control is achieved through outdoor air ventilation versus GUV_{222}, and how does this relationship vary with outdoor ozone concentration?

There are three important limitations to this work. First, we do not consider strategies for achieving the needed equivalent clean air delivery through the use of mechanical filtration methods, an alternate strategy that can be used to achieve ASHRAE Standard 241 without

generation of ozone or other byproducts [51, 52]. Second, we do not compare energy use for outdoor air ventilation versus GUV_{222}. We have previously analyzed the energy implications of varying outdoor air ventilation rates and different filtration strategies (including central HVAC filtration at MERV 8 and MERV 13 levels, as well as portable in-room air cleaners with HEPA filtration) across 13 U.S. cities representing different climate zones, using the similar prototype classroom design and building energy simulation methods [53]. However, that work did not evaluate the specific scenarios modeled here (i.e., comparison of GUV_{222} supplementation versus outdoor air-only compliance with ASHRAE 241). Energy analysis of these scenarios would require detailed consideration of climate-specific heating and cooling loads, which is beyond the scope of this ozone-focused study. Third, our analysis focuses only on analyzing indoor ozone concentrations and not ozone reaction byproducts. The lower outdoor air ventilation rates applied in the GUV_{222} scenario may lead to higher steady-state concentrations of any ozone reaction byproducts that are formed. A comprehensive assessment of byproduct concentrations would require detailed chemical modeling of indoor ozone chemistry, which is beyond our current scope.

Together, these objectives and limitations define the analytical scope of this whitepaper: to quantify the interrelated effects of GUV_{222} fluence rate, ozone generation, and air-disinfection efficacy, and to compare the resulting indoor ozone concentrations with those arising from increased outdoor air ventilation. The following sections establish the technical foundation for this comparison by reviewing the photolysis mechanisms of ozone formation under 222 nm irradiation, summarizing reported ozone emission and disinfection performance data, and outlining the modeling approach used.

II. GUV Irradiance and Impacts on Ozone Generation and Pathogen Inactivation

II.I Introduction to Irradiance

Understanding how irradiance, or the radiant flux incident on a flat surface, varies throughout a room illuminated by GUV is key to characterizing both ozone production and pathogen disinfection. The relationship between irradiance and ozone generation is linear (described in Section IV), allowing ozone generation to be estimated from average room irradiance. Pathogen inactivation, on the other hand, responds non-linearly to irradiance (described in Section V); meaning that accurate prediction of pathogen disinfection requires modeling the full spatial irradiance distribution. In this section, we describe the spatial distribution of irradiance produced by a GUV lamp.

The spatial extent of irradiation is often described in terms of "near-field" and "far-field." At sufficiently large distances, a GUV lamp behaves effectively as a point source [54]. Under photometric theory, irradiance (I) from a point source falls off according to the inverse-square law, $I \propto 1/Distance^2$. In practice, this approximation becomes accurate to within ~1% once the distance exceeds five times the lamp's largest dimension, and to within ~0.5% when the distance is greater than ten times that dimension [55]. For a tubular lamp, this criterion translates to distances of about 5 lamp lengths [55]. Closer in, however, the finite geometry of the lamp comes into play. In the near-field, a large fraction of the lamp spans the detector's view, and the intensity drop with distance is noticeably slower than $1/Distance^2$.

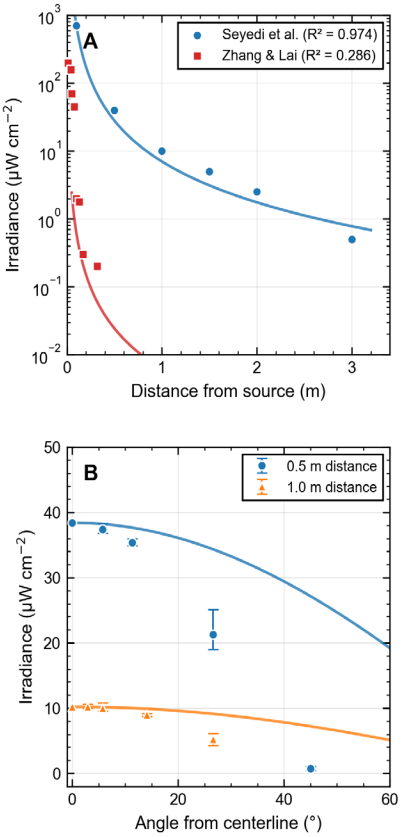

Figure 2. (A) Axial irradiance profiles for GUV222 lamps from Seyedi et al. (2023) and Zhang & Lai (2022) used to evaluate distance dependence relative to the inverse-square law. (B) Angular irradiance profiles measured at 0.5 m and 1.0 m

On top of distance effects, the angular distribution of emissions strongly shapes irradiance patterns. Germicidal lamps can often be approximated as Lambertian sources, meaning their radiant intensity, observed at an angle θ from the axis perpendicular to the emitting surface, scales with cosθ. In practical terms, irradiance is strongest directly under the lamp and diminishes at oblique angles. Most germicidal lamps adhere reasonably well to this Lambertian behavior unless modified by optics such as reflectors or collimators [56]. Taken together, these two geometric factors largely govern irradiance from GUV lamps: distance dependence (with near-field deviations from the inverse-square law) and angular distribution (Lambert's cosine law). Several groups have carried out direct irradiance measurements to quantify how actual GUV lamp fields fall off in both axial and radial directions. Zhang & Lai (2022) measured irradiance at the center of duct cross-sections for both GUV_{222} and GUV_{254} lamps, showing that both sources decayed in broadly similar ways. Irradiance dropped from hundreds of μW cm^{-2} at very short distances (e.g., 205.2 μW cm^{-2} at 5 mm) to near background levels at ~320 mm (0.2 μW cm^{-2}). This measured drop in irradiance over distance (red squares in Figure 2A) was slower than predicted (red line in Figure 2A) and had poor agreement with the inverse square law (R^2 = 0.286), likely due to the study's focus on very short distances from the lamp surface (5-320 mm) where near-field effects dominate and the finite lamp geometry is not well approximated as a point-source [57]. Seyedi et al. (2023) characterized the axial and radial irradiance fields from an Ushio B1 GUV_{222} lamp over distances up to 3 m. The measured axial irradiance (blue circles in Figure 2A) was in strong agreement with the inverse-square prediction (R^2 = 0.974), indicating that the lamp behaved as an effective point source beyond approximately 0.5 m from the lamp surface. At these distances, irradiance values were approximately 700 μW cm^{-2} at 0.1 m and 0.5 μW cm^{-2} at 3 m [24]. Radial measurements (Figure 2B) demonstrated decreasing irradiance with increasing

angle from the centerline, and closer proximity to the lamp produced greater deviations from an ideal Lambertian emitter (blue circles at 0.5 m) compared to the farther distance (orange triangles at 1.0 m) [24]. The solid curves in Figure 2B represent theoretical Lambertian profiles. The markers represent the average of four measurements taken at the same distance and angle; error bars show the range between minimum and maximum values. These observations indicate that while the lamp demonstrates Lambertian-like behavior at farther distances, empirical characterization is necessary to capture near-field geometric effects accurately.

We further describe the mathematical model developed by Link et al. (2023) to characterize the irradiance field of a KrCl* excimer GUV_{222} lamp out to 40 cm, as we applied this irradiance model for ozone generation calculations in Section IV and disinfection performance in Section VI [58]. Link et al. (2023) reported measured irradiance values of 105 W m^{-2} close to the lamp surface and 27 W m^{-2} at 5 cm. Beyond 5 cm, irradiance decreased with axial distance z following a power law relationship:

$$I[z] = \frac{I_0}{z^a} \tag{1}$$

with best-fit parameters a = 1.52 and I_0 = 0.286 W m^{a-2}. They further characterized angular emissions by rotating the lamp in 5° increments and measuring irradiance at multiple radial distances. Irradiance fell off steeply with polar angle, with most of the UV output confined to a half-angle (θ) of 55°.

To represent this behavior, Link et al. (2023) fitted a sigmoidal function defining irradiance as a function of both vertical (z) and radial (r) distance:

$$I[z,r] = \frac{I_0}{\left(\sqrt{\mathrm{z}^2 + r^2}\right)^a} \cdot \left(\mathrm{A} + \frac{(\mathrm{B} - \mathrm{A})}{1 + \exp\left(\frac{\frac{r}{\mathrm{z}} - \mathrm{b}}{\mathrm{c}}\right)} \right) \qquad \mathrm{Z} > \mathrm{Z}_{\mathrm{min}}$$

$$I[z,r] = 105 \frac{\mathrm{W}}{\mathrm{m}^2} \qquad \mathrm{Z} < \mathrm{Z}_{\mathrm{min}} \tag{2}$$

where A=0.00479, B=0.9809, b=0.7180 and c=0.1196.

For the ozone formation estimates we will conduct in Section IV, the average irradiance for the cone projected over the height (h) of the room is needed. The average irradiance for the volume of the cone can be calculated by integrating the total irradiance over all volumetric elements in cylindrical coordinates and dividing by the total volume:

$$I_{avg} = \frac{1}{V}\int_0^{2\pi}\int_0^{h}\int_0^{z\,tan(\theta_{max})} I[z,r]r\,dr\,dz\,d\emptyset \qquad (3)$$

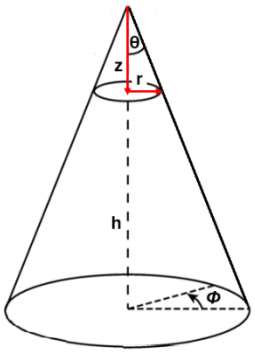

Figure 3. Cone geometry

where V is the total volume of the emission cone and θ_{max} represents the half-angle of the cone, which was 55° for the lamp tested Link, et al., 2023 [58]. Equation (3) yields a representative mean irradiance for the emission cone shown in Figure 3.

It is important to note that the irradiance field represented by this model does not include the influence of obstructions such as furniture or occupants, nor does it account for reflective contributions that arise under real-world conditions. Although far-UVC radiation is strongly absorbed by common indoor surfaces and attenuated by air [59], reflectivity is not universally negligible and can vary with wall and ceiling materials, furnishings, or surface coatings. Most indoor finishes reflect only about 10% of incident 222-nm radiation, and typically in a diffuse manner [59]. Ma et al. (2023) quantified reflections from sheets of 21 common materials under both filtered and unfiltered GUV_{222} lamps, as well as a GUV_{254} lamp (Figure 4) [60]. For organic materials commonly found in classroom environments, including wood, cardboard, polycarbonate, acrylic, and Formica laminate (typical desk and chair surfaces), reflectivity was consistently low, generally ranging from 3% to 10%. Typical inorganic surfaces such as marble and tile exhibited similarly low reflectance values. Fourteen of the 21 materials reflected least under filtered GUV_{222}, with average reflection values approximately 3.6% lower than the unfiltered lamp and 3.3% lower than the GUV_{254} lamp. In contrast, metals exhibited substantially higher reflectivity, ranging from

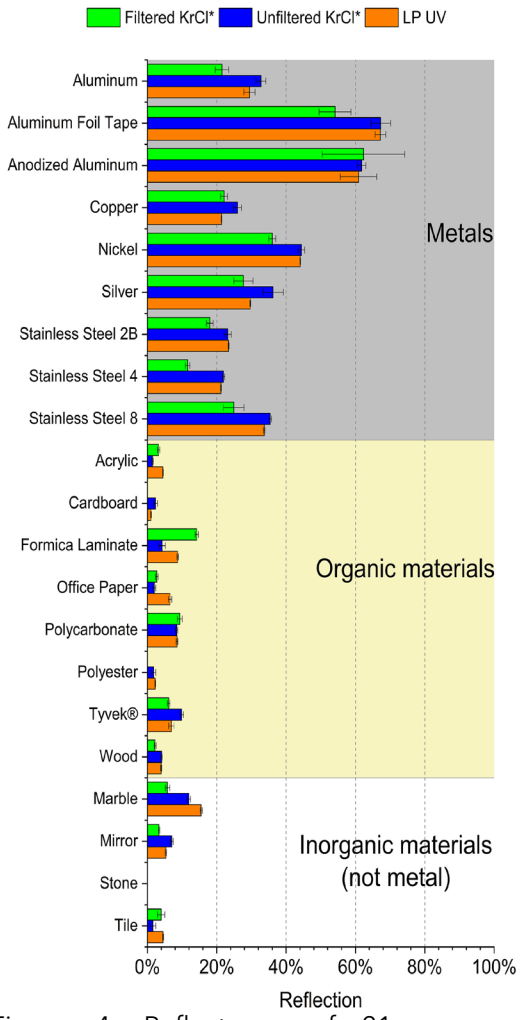

Figure 4. Reflectance of 21 common building materials under filtered and unfiltered 222-nm radiation compared to 254-nm UV reproduced from Ma et al.

approximately 12% for stainless steel #4 (filtered GUV_{222}) to as high as 67% for aluminum foil tape (unfiltered GUV_{222}). While metal components are present in classroom furniture (such as desk and chair legs or frames), the predominant surfaces that receive direct overhead irradiation from ceiling-mounted GUV_{222} fixtures, including desktops, chair seats, floors, and walls, are composed of low-reflectivity materials. Therefore, as will be described in Section II.II for irradiance simulation and corresponding ozone generation modeling, reflectance was assumed negligible and neglected [60].

Where reflections are minimal, GUV fields are dominated by direct line-of-sight contributions, and irradiance decays almost entirely with distance. This simplification is helpful for predictive modeling but comes with a trade-off, which is that surfaces outside the beam path receive little to no dose, leaving shaded zones without direct exposure. However, air mixing is expected to move air between shaded and irradiated air regions.

II.II Ozone Formation

The formation and removal of ozone under UV-C exposure follow well-known photochemical pathways described by the Chapman cycle, which has been central to atmospheric chemistry since it was first described in the early 20th century [61]. The principal reactions are summarized in Reactions (R1) through (R6), listed in the order they typically occur. Reactions (R1), (R2) and (R6) govern ozone formation, whereas (R3) through (R5) comprise the dominant loss mechanisms. In these reactions, M denotes a non-reactive collision partner that stabilizes activated species without undergoing chemical transformation. Ozone production initiates when molecular oxygen (O_2) absorbs UV photons between ~175 and 242 nm, yielding two ground-state oxygen atoms (R1). One of these atoms then pairs with another O_2 molecule to form ozone (O_3) (R2). Concurrently, ozone is susceptible to direct photolysis by photons at wavelengths below 300 nm, producing either excited-state $O(^1D)$ or ground-state $O(^3P)$ atoms (R3,R4). The $O(^1D)$ atoms rapidly relax to $O(^3P)$ through collisional quenching (R5). Ground-state oxygen can further deplete ozone by reacting with O_3 to form O_2 (R6) or reform ozone through R2. Under 222 nm irradiation, the production rate via R1-R2 typically exceeds the destruction rate via R3-R6, resulting in net ozone generation. This imbalance arises because 222 nm photons efficiently photolyze O_2, while the relatively low indoor ozone concentrations limit the second-order termination pathway in R6.

$$O_2 + h\nu_{(175\ \mathrm{nm} \le \lambda \le 242\ \mathrm{nm})} \rightarrow 2O(^3P) \quad \text{(R1)}$$

$$O(^3P) + O_2 + M \rightarrow O_3 + M \quad \text{(R2)}$$

$$O_3 + h\nu_{(\lambda \le 300\ \mathrm{nm})} \rightarrow O(^1D) + O_2 \quad \text{(R3)}$$

$$O_3 + h\nu_{(\lambda \le 300\ \mathrm{nm})} \rightarrow O_2 + O(^3P) \quad \text{(R4)}$$

$$O(^1D) + M \rightarrow O(^3P) + M \quad \text{(R5)}$$

$$O(^3P) + O_3 \rightarrow 2O_2 \quad \text{(R6)}$$

The net production rate for ozone generation scales linearly with the average irradiance of the GUV field, as described in Section V.II, and represents a key parameter governing the air-quality implications of GUV_{222} deployment indoors. Under controlled laboratory conditions, GUV_{222} lamps have been shown to generate ozone levels exceeding 100 ppb. In real indoor settings, however, the increases are typically much smaller—on the order of a few ppb—because of the combined effects of surface deposition, chemical reactions, and relatively low average irradiance. For example, measured increases include ~6.5 ppb in an office [62], ~5 ppb in a fragranced restroom (fragrance intentionally present to enable ozone–VOC byproduct analysis) [63], and ~0–10 ppb in a conference room [64]. Even these modest increments may be cause for concern, given the long periods of time people spend indoors and the cumulative nature of exposure [38].

II.III Ozone Reaction Byproducts

Ozone indoors is problematic not only because it is harmful in itself but also because it sets off a cascade of chemical reactions as shown below in R7-R10. Chief among these is the formation of hydroxyl (OH) radicals, which are even more reactive oxidants [65, 66]. OH radicals are produced primarily through ozonolysis of alkenes (R7) and through reaction of $O(^1D)$ with water vapor following ozone photolysis (R8). Ozonolysis yields are substantial, generally ~0.2–0.9 OH per reacted alkene molecule, depending on molecular structure and environmental conditions. Once formed, OH initiates a radical chain reaction, generating hydroperoxyl radicals (HO_2·, R9), which subsequently react with O_3 to regenerate OH (R10). Together, O_3 and OH rapidly oxidize volatile organic compounds (VOCs), producing oxygenated VOCs (OVOCs) such as formaldehyde and other low-molecular-weight carbonyls, and secondary organic aerosol (SOA), both of which have well-established links to adverse health effects [63, 67, 68].

$$\text{alkene} + O_3 \rightarrow OH\cdot + \text{other products} \quad \text{(R7)}$$

$$O(^1D) + H_2O \rightarrow 2OH\cdot \quad \text{(R8)}$$

$$OH\cdot + O_3 \rightarrow HO_2\cdot + O_2 \quad \text{(R9)}$$

$$HO_2\cdot + O_3 \rightarrow OH\cdot + O_2 \quad \text{(R10)}$$

Absent GUV_{222}, ozone is not produced by photochemistry indoors. Although ozone from outdoors can participate in a wide range of non-photolytic indoor reactions, the specific photolysis pathways that produce atomic oxygen from O_2 (λ < ~242 nm) and those that generate $O(^1D)$ (< ~330 nm) are effectively shut down indoors because the relevant wavelengths are strongly attenuated by atmospheric absorption and by standard window glass, respectively [69]. As a result, indoor OH production via ozone photolysis is typically

negligible without GUV_{222}, even though other ozone-initiated chemistry, such as ozonolysis of alkenes and surface reactions, remains important indoors.

Field studies have confirmed that GUV_{222}-induced ozone formation can initiate secondary chemistry indoors [67, 70-72]. Link et al. (2024) reported measurable lamp-generated ozone that engaged in secondary chemistry, altering VOC composition and rapidly producing ultrafine particles in a restroom. Particle number concentrations increased sharply within 30 minutes of lamp activation and plateaued in the absence of forced air circulation after approximately two hours [63].

Additional sinks further impact indoor ozone levels. Reaction with surfaces, including building materials, furnishings, and occupants, generally represents the dominant loss pathway [38, 73]. When indoor ozone concentrations exceed outdoor levels, ventilation provides an additional removal mechanism. The extent of GUV_{222}-initiated chemistry is expected to vary with ventilation rates, the abundance and types of VOC precursors, and surface reactivity [63]. In densely occupied spaces, deposition onto occupants can dominate ozone losses [73]. Ozone reactions with human skin lipids, particularly squalene and unsaturated fatty acids, are a potent source of secondary pollutants including carbonyls, dicarbonyls, hydroxycarbonyls, and aerosols [74-76]. Laboratory studies have demonstrated that ozone reactions with skin-oiled clothing generate volatile organic compounds including acetone, 6-methyl-5-hepten-2-one, nonanal, and decanal [75], as well as ultrafine particles [75] and nanocluster aerosols [77].

Risk of exposure to ozone reaction byproducts increases when ventilation is poor. Several studies have cautioned against operating GUV_{222} in low-ventilation spaces [62, 78, 79]. When air exchange with outdoors is limited, GUV_{222}-generated ozone can accumulate and react with VOCs and surfaces to produce harmful byproducts. Lower ventilation rates have been linked to higher ultrafine particle concentrations from ozone chemistry, even under comparable ozone levels [80]. There is no established minimum ventilation rate below which byproduct formation becomes unacceptable, and available evidence suggests that the threshold likely depends on room size, precursor VOC concentrations, and surface reactivity rather than a single universal air change rate (ACR) value. Rai et al. (2013) observed that particles larger than 10 nm formed via ozone reactions with skin-oiled fabrics at an ACR of 0.5 h^{-1}, but not at 2.7 h^{-1}, despite similar ozone concentrations [81]. Link et al. (2024) reported that GUV_{222}-initiated VOC oxidation products decreased from ~75 ppb to ~60 ppb when ventilation increased from ~1 to ~2 h^{-1}, although byproduct formation remained significant at both rates [63].

These findings highlight a potential trade-off in infection control strategies. If outdoor air ventilation is intentionally reduced in reliance on GUV_{222} for pathogen inactivation, there is a risk of increased occupant exposure to ozone and its reaction byproducts. Taken together, the air-quality impacts of GUV_{222} are strongly modulated by ventilation rates, occupancy density, and outdoor ozone concentration, underscoring the need for detailed modeling to predict how these factors affect outcomes. As noted in Section II.V, the scope of this study is limited to ozone modeling. While secondary reaction byproducts are acknowledged as

important, their formation pathways and magnitudes depend strongly on the specific indoor chemical environment and are beyond the scope of this report.

II.IV Other Photolysis Impacts

Beyond ozone-driven chemistry, energetic UV-C photons at 222 nm can directly photolyze numerous indoor VOCs, including peroxides, carbonyls, and other oxygenated intermediates, which increases radical production and can drive secondary pollutant formation [82]. Several studies report higher photolysis rates and quantum yields at 222 nm relative to 254 nm for representative organics [83], although the extent to which these accelerated rates influence indoor air remains uncertain. Species such as NO_2 and HONO also photolyze efficiently at this wavelength, altering OH production and radical cycling [67].

Goss & Kroll (2025) examined aerosol formation under an Ushio Care222 B1 lamp to separate the effects of direct 222 nm photochemistry from ozone-driven oxidation. They found that most secondary chemistry, including SOA formation, aerosol yield, and composition, was governed mainly by ozone chemistry and that direct VOC photolysis played a comparatively minor role [70]. The one consistent departure from this trend involved new particle formation (NPF), which increased substantially at high irradiance (45 μW cm^{-2}) in a 0.15 m^3 chamber when VOCs were present. Blank experiments with ultra-zero air showed no increase, implicating gas-phase organic photolysis in NPF initiation. The underlying mechanism remains unresolved. Even so, the authors noted that realistic indoor irradiance (3.9 μW cm^{-2}) coupled with slow oxidation and rapid particle deposition to surfaces would likely suppress NPF [70].

Taken together, the available evidence indicates that ozone formation and ozone-initiated chemistry dominate indoor secondary pollutant production associated with GUV_{222}, while the contribution of direct photolysis of VOCs is still being evaluated [58, 63, 70].

II.V Pathogen Inactivation

Viral susceptibility to UV-C irradiation depends strongly on genome structure. Larger genomes present more molecular targets for photochemical damage, generally raising the likelihood of functional inactivation [84-86]. Single-stranded viruses are also more susceptible because they possess only one copy of their genetic material. Coronaviruses, which carry the largest genomes among single-stranded RNA (ssRNA) viruses—ranging from 27.3 kb (HuCoV-229E) to 31.3 kb (MHV) (Table 3)—are particularly vulnerable to UV-C exposure. For example, SARS-CoV-2 possesses a 29.8 kb ssRNA genome, approximately 8-fold larger than non-enveloped ssRNA bacteriophages such as MS2 (3.6 kb) and Qβ (4.2 kb), and more than twice the size of segmented ssRNA viruses like Influenza A H1N1 (13.5 kb). By contrast, double-stranded DNA (dsDNA) viruses, including both non-enveloped bacteriophages (T1: 48.8 kb) and human adenoviruses (Type 2: 35.9 kb), often display greater resistance to UV-C, partly because their redundant genetic material offers protection and because host-cell repair processes can undo UV-induced lesions [87-89]. Despite having similar or even larger genome sizes than coronaviruses, dsDNA viruses benefit from the structural stability of

double-stranded nucleic acids and access to cellular repair mechanisms that are unavailable to RNA viruses.

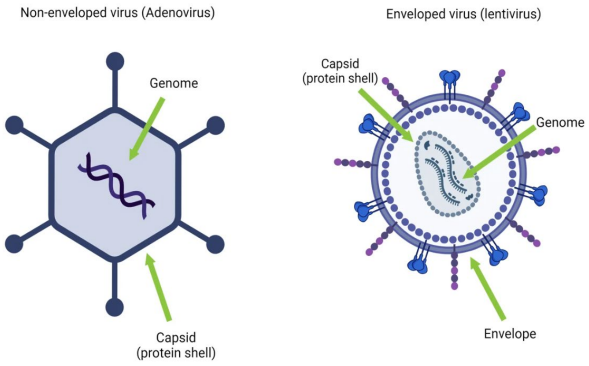

Figure 5. A non-enveloped virus (left) and an enveloped virus (right). Reproduced from [90].

Structural features further shape viral stability. Non-enveloped viruses encase their genome in a protein capsid, while enveloped viruses are surrounded by an additional lipid–protein membrane [91]. This envelope aids immune invasion but also makes them more prone to stressors such as pH extremes, heat, desiccation, and chemical disinfectants. Despite this, current evidence indicates that the envelope itself has a limited role in determining UV-C susceptibility [3]. Table 3 summarizes the relevant genetic attributes of representative human viruses and bacteriophages evaluated in this context.

Table 3. Genetic properties of representative human viruses and bacteriophages (Adapted from Blatchley III et al. (2023)[3]).

Pathogen	Genome Type	Enveloped or non-enveloped	Genome size (kilobases or kilobase pairs)
Adenovirus (Type 2)	dsDNA	Non-enveloped	35.9 kb
Bacteriophage MS2	ssRNA	Non-enveloped	3.6 kb
Bacteriophage Qβ	ssRNA	Non-enveloped	4.2 kb
Bacteriophage T1	dsDNA	Non-enveloped	48.8 kb
Bacteriophage T1UV	dsDNA	Non-enveloped	(Assumed similar to T1)
Bacteriophage φ6	Segmented dsRNA	Enveloped	13.4 kb
HuCoV-229E	ssRNA	Enveloped	27.3 kb
HuCoV-OC43	ssRNA	Enveloped	30.7 kb
Influenza A (H1N1)	Segmented ssRNA	Enveloped	13.5 kb
MERS	ssRNA	Enveloped	30.1 kb
MHV	ssRNA	Enveloped	31.3 kb
SARS-CoV-1	ssRNA	Enveloped	29.7 kb
SARS-CoV-2	ssRNA	Enveloped	29.8 kb

GUV inactivation of airborne pathogens is commonly modeled as a first-order process. Although biphasic behavior can occur, with a small subpopulation (<1%) exhibiting increased resistance, more than 90% of the total inactivation typically occurs in the initial decay regime. First-order kinetics therefore provide an appropriate and practical representation for most GUV applications. The dose–response relationship is expressed as:

$$\ln \frac{S_i}{S_0} = -k \cdot D \tag{4}$$

where S_i represents the concentration of infectious microorganisms at time i per unit area of volume, S_0 is the initial concertation of infectious microorganisms per unit area of volume, k is the first-order inactivation rate constant in base e (cm^2/mJ) and D is the delivered UV-C dose (mJ/cm^2), calculated as the product of irradiance I ($\mu W/cm^2$) and exposure time t (s), with proper unit conversion (1 mJ = 1000 μJ).

Published GUV_{222} inactivation rate constants vary substantially across pathogens and experimental systems. There is no definitive consensus on what value to use when conducting simulations to design systems, largely due to differences in aerosolization methods, environmental conditions, and quantification techniques. Current guidance favors either adopting the lower bound of reported values for conservative design or using the full reported range to represent uncertainty [92]. Table 4 compiles available k values for representative airborne viruses and bacteria measured under aerosol exposure [92].

Table 4. Reported GUV_{222} inactivation rate constants for representative airborne pathogens, where the inactivation rate was measured for the pathogen in an aerosol. The first order rate constant is reported as k_1 and, where applicable, a second first-order rate constant representing the slower phase of bi-phasic inactivation is reported as k_2.

Pathogen	Genome type	Envelope status	k_1 (cm^2/mJ)	k_2 (cm^2/mJ)	Quantification method	Reference
Viruses						
Bacteriophage MS2	ssRNA+	Non-enveloped	0.22		NA	[93]
Bacteriophage MS2	ssRNA+	Non-enveloped	0.41		NA	[93]
Bacteriophage MS2	ssRNA+	Non-enveloped	5.75		CFU	[94]
Bacteriophage P22	dsDNA	Non-enveloped	3		PFU	[57]
Bacteriophage P22	dsDNA	Non-enveloped	17.14		CFU	[94]
Bacteriophage Phi6	dsRNA	Enveloped	20.08		CFU	[94]
Human coronavirus	ssRNA+	Enveloped	1.14		TCID50	[95]
Human coronavirus	ssRNA+	Enveloped	4.11		TCID50	[26]
Human coronavirus	ssRNA+	Enveloped	5.9		TCID50	[26]
Human coronavirus	ssRNA+	Enveloped	7		TCID50	[96]
Human coronavirus	ssRNA+	Enveloped	10.5		TCID50	[96]
Human coronavirus	ssRNA+	Enveloped	12.4		TCID50	[25]
Human coronavirus	ssRNA+	Enveloped	14.26		TCID50	[97]
Influenza virus	ssRNA-	Enveloped	1.8		NA	[25]
Influenza virus	ssRNA-	Enveloped	20.06	2.3	TCID50	[98]
Murine norovirus	ssRNA+	Non-enveloped	2.36	0.35	TCID50	[98]

Pathogen	Genome type	Envelope status	k_1 (cm^2/mJ)	k_2 (cm^2/mJ)	Quantification method	Reference
Bacteria						
Escherichia coli			1.14		CFU	[99]
Escherichia coli			4.9		CFU	[57]
Escherichia coli			21.93		CFU	[94]
Pseudomonas alcaligenes			7.5		CFU	[57]
Salmonella enterica			4.97		CFU	[94]
Serratia marcescens			3.3		CFU	[57]
S. aureus			20.8		CFU	[100]
S. epidermis			3.05		CFU	[94]
S. epidermis			6.3		CFU	[57]

II.VI Impact of Mixing

Spatial variability in irradiance is inherently linked to air mixing, which governs how rapidly exhaled pathogens are transported throughout an indoor environment. As discussed in Section II.V, the inactivation of pathogens by GUV follows an exponential dose-response relationship. This means that pathogens passing closest to the lamp are inactivated most rapidly, while those in regions with lower irradiance are inactivated more slowly. How well GUV performs, therefore, depends on how the pathogen emission from the source(s) mixes within the GUV field. Mixing time is shaped by airflow patterns, which in turn depend on ventilation strategies (e.g., displacement vs. mixing), room geometry, and internal heat sources [101, 102]. For upper-room GUV_{254}, this has long been recognized as central, since air exchange between the breathing zone and the irradiated zone controls overall disinfection efficiency [103, 104]. GUV_{222} is often assumed to be less sensitive to mixing, on the premise that irradiation is more evenly spread throughout the space. Although the whole-room approach of GUV_{222} will reduce sensitivity to mixing, irradiance fields remain highly variable, meaning airflow patterns still play a role in disinfection. Fans can be added to improve mixing. Due to the importance of this parameter, our disinfection rate calculations in Section VI include a simplified model to evaluate the impact of mixing time.

It should be noted that mixing does not impact ozone generation rates, since ozone production is governed by fundamentally different physics than pathogen inactivation. As will be described in Section V. II, ozone formation from GUV_{222} depends solely on oxygen photolysis (Equation 10), which is determined by the local photon flux and near-uniform concentration of molecular oxygen in indoor air. Unlike pathogen-laden aerosols—which must physically transit through the irradiance field to be inactivated—molecular oxygen is uniformly abundant throughout the room at approximately 21% by volume (~8.7 mol m^{-3}). The rate of oxygen consumption via photolysis is negligible relative to the total oxygen present; even at maximum irradiance, O_2 depletion is typically less than 0.001% and is continuously replenished by ventilation. Consequently, oxygen concentration remains effectively homogeneous throughout the space, and the total ozone generation rate is simply the volume integral of the local photolysis rate over the irradiated volume—independent of how

air circulates through that volume. In contrast, pathogen inactivation efficiency is strongly mixing-dependent because a finite number of viable pathogens must be physically transported through a highly variable irradiance field.

III. Public health impacts of indoor ozone exposure

III.I Ozone

A substantial body of epidemiological evidence has established ozone as a consistent driver of adverse health outcomes. Epidemiological studies typically evaluate the relationship between mortality and ambient outdoor ozone concentrations, as outdoor ozone data are the most widely available exposure metric, even though people spend ~90% of their time indoors [105]. However, outdoor ozone concentrations are a reasonable proxy for indoor exposure, since outdoor ozone largely determines indoor ozone concentrations.

Long-term exposure has been linked to acute respiratory irritation, impaired lung function, and exacerbation of asthma, with children, older adults, and individuals with pre-existing conditions most at risk [106]. Beyond the lungs, ozone induces oxidative stress and inflammatory responses that spill over into systemic effects, contributing to cardiovascular morbidity [107]. Syntheses of this literature highlight the broad public health toll: increases in respiratory-related hospitalizations, asthma emergencies, restricted activity days, lost school attendance, and premature mortality [108, 109].

Meta-analyses converge on statistically robust mortality effects, and have demonstrated that daily mortality rises by ~0.87% for every 10 ppb increase in mean daily ambient ozone [110], and by ~0.39–0.41% for each 10 ppb increase in the 1 h daily maximum [111, 112]. Subsequent studies report similar ranges, from a 0.45% increase per 5 ppb step in short-term averages [113] to nearly 4% per 25 ppb rise [113]. A recent study reported that for a 10 ppb increase in ozone resulted in a risk ratio of 1.12 [1.08-1.12] [114]. Taken together, these findings demonstrate that even small increases in ambient ozone translate into measurable excess mortality.

III.II Ozone Reaction Byproducts

As discussed in Section II.III, ozone indoors triggers a cascade of secondary chemistry, yielding a suite of byproducts with toxicological relevance of their own. In some cases, these reaction products may carry greater health implications than ozone itself [115, 116]. The most important groups of compounds include aldehydes (notably formaldehyde and acetaldehyde), organic acids, carbonyls, and SOA formed via ozone–terpene reactions. Ultrafine particles generated in these processes can build up to high number concentrations, especially in environments rich in precursors from cleaning agents, air fresheners, or routine occupant activities.

Health impacts linked to these byproducts are wide-ranging. Formaldehyde is a well-known respiratory irritant and human carcinogen [117]. Acetaldehyde contributes to mucosal irritation and systemic toxicity [118]. Freshly formed SOA and ultrafine particles can provoke

airway inflammation, worsen asthma, and impair lung function, while also driving systemic oxidative stress that contributes to adverse cardiovascular outcomes [45, 119, 120].

Evidence from epidemiological and toxicological studies shows that these secondary products add to, rather than replace, the health burden of ozone itself. Chamber experiments demonstrate that ozone–limonene reactions alone can generate formaldehyde and ultrafine particle concentrations well above health-based benchmarks [121-123]. Field studies in offices, classrooms, and homes confirm that these processes occur under everyday conditions [124].

In short, the risks of indoor ozone are not solely dependent on the parent gas alone. Instead, they stem from a complex mixture of ozone and its byproducts, which together amplify the adverse health impacts of indoor exposure.

IV. Modeling an example classroom application

Lamp placement strongly influences performance because disinfection efficacy scales with the irradiated volume. We evaluated a three-lamp configuration in which each lamp was represented by a conical emission field (θ_{max}=55°), under two different ceiling heights of 3.05 m and 2.45 m. The configuration was modeled with one lamp at the center of the room projecting vertically downward, and two lamps along the centerline, each tilted 35° from vertical (Figure 6). This arrangement was selected to increase spatial coverage while limiting unnecessary overlap between emission fields. For a ceiling height of 3.05 m, the combined irradiated volume was approximately 181 m^3 of the total 272 m^3 room volume. For a 2.45 m ceiling, the irradiated volume was 94 m^3 of 218 m^3.

Although the outer cones intersect geometrically with the central cone, this overlap was not explicitly accounted for because irradiance declines with both distance and off-axis angle; contributions in overlapping regions are therefore small relative to regions nearer the lamp axis. For the outer lamps, a fraction of the emission cone is truncated by the walls and floor—approximately 18% for a 3.05 m ceiling and 15% for a 2.45 m ceiling. This truncation formally reduces the volume contributing to ozone formation and pathogen inactivation. However, because irradiance in these peripheral regions is low, the impact on predicted ozone production and disinfection is expected to be minor. Accordingly, truncation effects were neglected to simplify the analysis. A further limitation of our approach is that it does not account for obstructions such as furniture or occupants, which would reduce the effective radiated volume, or for surface reflections, which could enhance the effective irradiated volume. Obstructions and reflections from surfaces would generally occur in regions of lower irradiance farther from the lamp, so their influence on ozone generation and pathogen inactivation is expected to be limited.

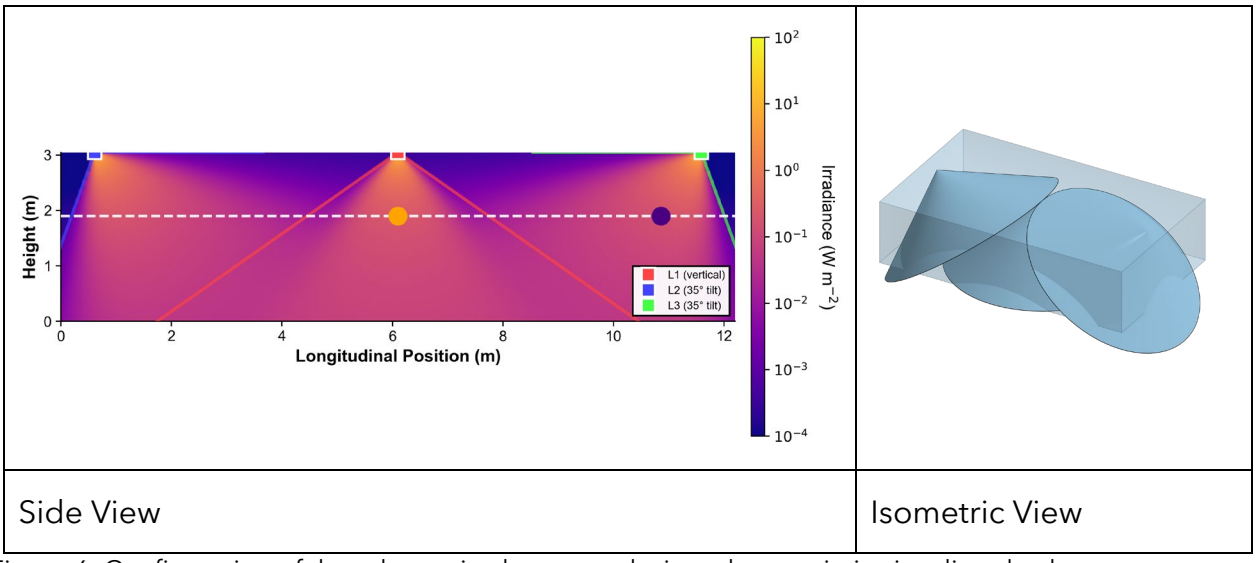

Figure 6. Configuration of three lamps in classroom designed to maximize irradiated volume.

As described in Section II.I, our modeling framework builds on the mathematical formulation presented by Link et al. (2023) for calculating the spatial irradiance distribution from GUV_{222} lamps. For the 3.05 m ceiling case, we applied a scaling (dimming) factor of 0.43 to align the predicted irradiance distribution with the output of an Ushio B1 lamp. The derivation of this factor is provided in Appendix A. As described in Appendix A, the maximum irradiance of the Ushio B1 lamp is 12.1 μW cm^{-2} at 1 m from the source. This classifies the lamp as risk group 0 under ANSI/IES RP 27.1-22 as described in Section I.III. In order to assess compliance with ANSI/UL 8802, we also need to consider the irradiance 1.9 m from the floor (white dashed line in Figure 6). In the center of the room (orange circle in Figure 6), the irradiance is 9.8 μW cm^{-2}, which is within the limit of skin safety for a downward facing lamp (Table 5). For the tilted lamps on the sides of the room, we must also consider eye safety. The highest irradiance at a height of 1.9 m is along the lamp centerline at a distance of 1.28 m from the source (dark purple circle in Figure 6). At this point, the irradiance on a plane perpendicular to the lamp is estimated at 8.5 μW cm^{-2}. Using geometric relationships, we calculated the irradiance on the vertical plane—the value relevant for eye safety—to be 4.9 μW cm^{-2}, which is below the eye exposure limit of 5.6 μW cm^{-2}. Thus, this modeled scenario is within the eye and skin safety limits of ANSI/IES RP 27.1-22 and ANSI/UL 8802 as described in Section I.III.

For the 2.45 m ceiling configuration, the 1.9 m evaluation height is only 0.55 m from the source. To satisfy ANSI/UL 8802 under the 2.45 m ceiling condition, we uniformly scaled the irradiance field to 19% of the nominal output (Table 5). While this scaling does not correspond to a specific commercial product rating, it represents a technically feasible operating condition, as lamp output can be designed or electronically controlled to achieve a prescribed irradiance.

These two modeled scenarios intentionally push toward the upper end of permissible GUV irradiance for skin and eye safety. Although many lamp models operate at substantially lower

outputs, we selected a configuration close to the exposure limits to characterize the highest realistic levels of ozone generation and disinfection effectiveness.

Table 5. Scaling factors for 10 ft ceiling and 8 ft ceiling

Ceiling Height	Distance from lamp 1.9 m above the floor (m)	Link et al predicted irradiance for skin exposure 1.9 m above the floor ($\mu W/cm^2$)	Link et al predicted irradiance for eye exposure 1.9 m above the floor ($\mu W/cm^2$)	Scaling factor applied to Link et al irradiance map	Modeled irradiance for skin exposure 1.9 m above the floor ($\mu W/cm^2$)	Modeled irradiance for eye exposure 1.9 m above the floor ($\mu W/cm^2$)	Notes
10 ft (3.05 m)	1.15	27.98	11.27	0.433	9.8 (limit 15.9)	4.85 (limit 5.6)	Representative of Ushio B1 lamp
8 ft (2.45 m)	0.55	69.43	28.83	0.19	13.2 (limit 15.9)	5.5 (limit 5.6)	Dimmed to meet ANSI/UL 8802

V. Modeling indoor ozone concentration

To evaluate the ozone-related implications of outdoor air ventilation versus GUV_{222} for meeting ASHRAE Standard 241, we conducted a modeling analysis for an example classroom application. We first assessed the indoor ozone concentration that would result from using only outdoor air at an air change rate of 10.3 h^{-1} to meet ECA requirements of Standard 241. An air change rate of 10.3 h^{-1} corresponds to replacing the room air approximately every six minutes. This scenario was contrasted with an alternate case applying the ASHRAE Standard 62.1 outdoor air rate of 3.5 h^{-1} and the three GUV_{222} lamps as described in Section IV. To capture regional variability, we selected three California cities—Oakland, Sacramento, and Riverside—using CalEnviroScreen, a statewide mapping tool developed by the Office of Environmental Health Hazard Assessment to assess cumulative environmental burdens and community vulnerability [125]. These cities represent low, moderate, and high ambient ozone environments. Finally, we calculated the ECA for the Standard 62.1 outdoor air plus GUV_{222} scenario and compared it to the ASHRAE 241 outdoor air scenario. This comparison provides a quantitative framework for evaluating trade-offs between ventilation-based and GUV_{222}-based disinfection strategies in relation to both indoor ozone exposure and ECA delivered.

V.I Ozone Concentration Mass Balance Model

We modeled time-resolved indoor ozone concentrations in a representative classroom using a well-mixed box framework. The governing differential equation accounted for ventilation, deposition to human occupants and indoor surfaces, and an internal ozone source term used to model GUV_{222} emissions:

$$V\frac{dC_{in,O_3}(t)}{dt} = Q\left[C_{out,O_3}(t) - C_{in,O_3}(t)\right] - N\,v_{d,h}\,A_h\,C_{in,O_3}(t) - v_{d,sr}\,A_{sr}\,C_{in,O_3}(t) + S_{O_3}(t) \quad (5)$$

where, C_{out,O_3} and C_{in,O_3} are the outdoor and indoor ozone concentrations, respectively, V is the volume of the classroom (272 m^3 for a 3.05 m ceiling; 218 m^3 for a 2.45 m ceiling), Q is the outdoor air ventilation rate, and $S_{O3}\,(t)$ represents a time-dependent source term attributed to GUV_{222}. The terms A_h (1.14 m^2 per person) and A_{sr} (296.7 m^2 per classroom) denote the effective surface areas of human occupants and indoor surfaces, respectively, while $v_{d,h}$ and $v_{d,sr}$ represent ozone deposition velocities onto human surfaces and indoor surfaces. Ozone deposition velocities of 16.2 m h^{-1} for human surfaces and 0.985 m h^{-1} for indoor surfaces were derived from field data collected in an occupied classroom (see Appendix B). Ozone uptake via respiration was excluded, as prior studies indicate that its contribution is negligible relative to deposition onto human bodies and other indoor surfaces [126]. At the start of each simulation, indoor ozone concentrations were assumed equal to outdoor levels. Indoor ozone was then calculated forward in time using Euler's method with a 5-minute time step.

To capture the influence of regional ozone variability on indoor air chemistry, we selected three California locations representing distinct outdoor ozone regimes: Oakland (low-ozone), Sacramento (moderate-ozone), and Riverside (high-ozone). Hourly ambient ozone concentrations data for each site were obtained from the CARB database for the period January 1 to December 31, 2024 [127]. These data served as the input for the outdoor ozone concentration into Equation 5.

Ventilation rates were calculated following the respective formulas and guidance outlined in ASHRAE Standards 62.1 and 241. Under ASHRAE 62.1, the total outdoor airflow rate was calculated as the sum of people-based and area-based components:

$$Q = R_p \cdot N + R_a \cdot A_f \quad (6)$$

where R_p is the recommended outdoor air rate per person (5 L s^{-1} per person for classrooms with occupants aged 9 and above), R_a is the area-based rate (0.6 L s^{-1} m^{-2}), N is the number of occupants (assumed to be 31 based on a density of 35 persons per 100 m^2), and A_f is the floor area of the classroom (89 m^2).

ASHRAE Standard 241 specifies an ECA rate of 20 L s^{-1} per person, leading to the following expression for ventilation rate:

$$Q = ECA \cdot N \quad (7)$$

To assess the impact of GUV_{222} lighting on indoor ozone concentrations, we simulated two identical classrooms: one ventilated with 100% outdoor air to meet ASHRAE Standard 241,

and the other under ASHRAE Standard 62.1 supplemented by GUV_{222} devices. All physical and operational parameters, including room volume, geometry, occupancy patterns, and surface properties, were held constant across both scenarios. The only differences were the outdoor-air change rate and the presence of an indoor ozone source from GUV_{222} in the ASHRAE 62.1 scenario. Occupancy patterns, ventilation rates, and GUV_{222} lamp operation were modeled using the bell schedule of a typical elementary school (Table 6).

Table 6. Occupancy patterns, ventilation rates, and GUV_{222} lamp operation daily schedule.

Time	Occupancy	ASHRAE 241 with outdoor air only	ASHRAE 241 with outdoor air per ASHRAE 62.1 + GUV_{222}	
		Outdoor air rate (from equation 7)	Outdoor air rate (from equation 6)	GUV_{222} status
8:00	1	624 L s^{-1}	210 L s^{-1}	ON
8:30	31	624 L s^{-1}	210 L s^{-1}	ON
11:30	1	624 L s^{-1}	210 L s^{-1}	ON
12:30	31	624 L s^{-1}	210 L s^{-1}	ON
15:00	1	624 L s^{-1}	210 L s^{-1}	ON
16:00	0	12.7* L s^{-1}	12.7* L s^{-1}	OFF

* When the HVAC system was off, an air change rate of 0.21 h^{-1} was assumed [128].

V.II Simulation GUV_{222} Irradiance and Ozone Generation

As introduced in Section VI, we constructed a three-dimensional irradiance profile following the methodology proposed by Link et al. (2023) [58]. In this framework, the irradiance I[z,r] is described by a sigmoidal fit, where z represents the vertical distance from the source and r represents the radial distance from the beam's central axis, as defined earlier in Equation 2.

With the spatial irradiance distribution defined, the average irradiance within the emission cone was obtained using the volume integral in Equation 3. Each lamp was assumed to be ceiling mounted, with the emission cone extending from the fixture to the floor. For a ceiling height of 3.05 m and a half-angle of 55°, the maximum radial extent (h $\tan(\theta_{max})$) is 4.35 m, yielding a cone volume of 60.6 m^3. For a ceiling height of 2.45 m, the corresponding radius is 3.5 m and the cone volume is 31.4 m^3. In both our model and Link et al. (2023), the effect of surface reflections was assumed to be negligible and neglected [58], a choice supported by the low reflectance values reported earlier (Section II.I; Figure 4).

The calculated average irradiance I_{avg} for each Ushio B1 lamp, modeled as described in Section II.I was 1.016 μW cm^{-2} for the 3.05 ceiling height and 0.622 μW cm^{-2} for the 2.45 ceiling height. The corresponding photon flux *F* was then calculated as:

$$F = \frac{I_{avg}}{E} = \frac{I_{avg}}{\frac{hc}{\lambda}} \quad (8)$$

where h is Planck's constant (J s), *c* is the speed of light (m s^{-1}) and λ is the wavelength (m). The photon energy (*E*) was determined from $E=hc/\lambda$ for λ=222 nm; yielding $E=8.96 \times 10^{-19}$ J. The first-order rate constant for molecular oxygen photolysis, j_{O_2} was then calculated using the following integral:

$$j_{O_2} = \int \sigma_{O_2} \phi_{O_2} F d\lambda \quad (9)$$

where σ_{O_2} is the absorption cross section (cm^2) and ϕ_{O_2} is the quantum yield. An effective absorption cross section of σ_{O_2} = 4.30 × 10^{-24} cm^2 was applied over the 210–230 nm wavelength range [58] and the quantum yield ϕ_{O_2} was taken to be unity across this spectral range [129]. Using the calculated photolysis rate, the ozone production rate was determined by:

$$\frac{d[O_3]}{dt} = 2 j_{O_2} [O_2] \quad (10)$$

where $[O_2]$ is the ambient oxygen concentration. The factor of 2 accounts for the two ozone molecules produced per O_2 photolysis event under this reaction pathway. The result from Equation 10 was calculated as a constant rate per lamp. The result was multiplied by the number of lamps modeled in the classroom and implemented as the source term $S_{O_3}(t)$ in Equation 5. The time varying nature of $S_{O_3}(t)$ represents a step function for lamps on or lamps off, which was set by the occupancy schedule.

The modeled ozone generation rate was 0.88 mg h^{-1} per ceiling-mounted lamp for the 3.05 m ceiling (lamp operated at 43% of full output) and 0.28 mg h^{-1} for the 2.45 m ceiling when output was reduced to 19% to satisfy ANSI/UL 8802 exposure limits.

We then applied this ozone generation rate for the modeled scenario as the indoor source term in Equation 5 and calculate the indoor ozone concentration for each hour of the year for the three different cities modeled. For the year analyzed, mean outdoor ozone concentrations averaged 27.28 ± 9.16 ppb in Oakland, 37.38 ± 14.64 ppb in Sacramento, and 51.73 ± 25.25 ppb in Riverside during school hours on weekdays. Excluding summer break periods yielded corresponding averages of 28.21 ± 9.57 ppb, 34.83 ± 13.56 ppb, and 45.89 ± 22.52 ppb, respectively.

The results show indoor ozone concentration as a function of outdoor ozone concentration for both the ASHRAE 241 outdoor air ventilation scenario (Figure 7, triangles) and ASHRAE 62.1 ventilation plus GUV_{222} (Figure 7, circles) for a ceiling height of 3.05 m (Figure 7, left) and a ceiling height of 2.45 (Figure 7, right). The threshold outdoor concentration (red cross mark) above which ASHRAE 241 outdoor air ventilation results in higher indoor ozone than ASHRAE 62.1 ventilation plus GUV_{222} was 10.7 ppb for the 3.05 m ceiling and 6.8 ppb for the 2.45 m ceiling.

The results indicate that ventilating in accordance with ASHRAE 62.1 while operating three GUV_{222} lamps yields lower indoor ozone concentrations in the modeled classroom than increasing outdoor air ventilation to meet ASHRAE 241 ECA requirements. This finding was consistent across all three California cities evaluated. The results further show that the increased outdoor air scenario would produce lower indoor ozone concentrations only if the average outdoor ozone concentration were below 10.7 ppb for the 3.05 m ceiling and 6.8 ppb for the 2.45 m ceiling. By comparison, estimated U.S. background ozone concentrations – defined as ozone attributable to natural sources and international transport, excluding domestic anthropogenic emissions – typically range from 20 to 45 ppb during spring and summer months, with lower values (~27 ppb) at low-altitude sites and higher values (~40 ppb) at high-altitude western locations [130-133]. Even the lower bound of these estimates substantially exceeds 10.7 ppb, indicating that under virtually all realistic ambient ozone conditions in the U.S., the GUV_{222} scenario will result in lower indoor ozone exposure than the strategy of increasing outdoor air ventilation rates to meet ASHRAE 241. For a complete comparison of the two approaches, however, it is also necessary to evaluate and compare the effective clean air delivered by each scenario, which we address in the following section.

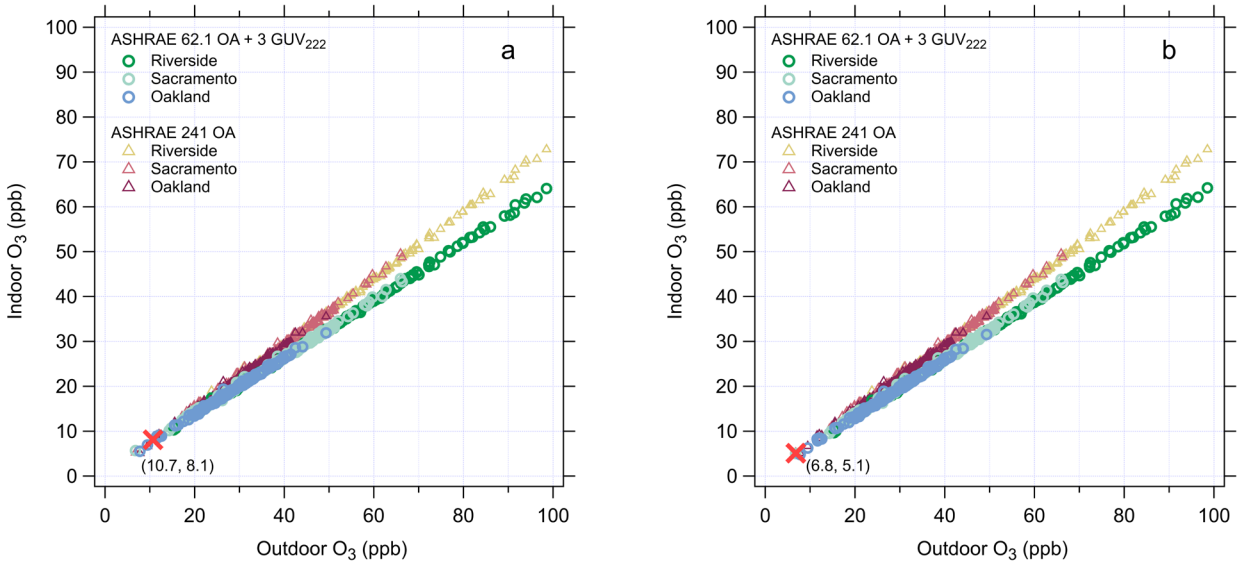

Figure 7. Modeled indoor ozone concentrations for two scenarios: 1) ASHRAE 62.1 outdoor air ventilation combined with ozone generation from three GUV222 lamps and 2) ASHRAE 241 requirements met via outdoor air ventilation. Results are shown for (a) a 3.05 m ceiling height (corresponding to a 2.64 mg h-1 ozone generation rate) and (b) a 2.45 m ceiling height (corresponding to a 0.84 mg h^{-1} ozone generation rate).

VI. Simulation GUV_{222} Clean Air Delivery Rate

The ozone generation rate from GUV_{222} was estimated from the average irradiance across the lamp's projected emission cone, since ozone generation scales linearly with irradiance. Pathogen inactivation, however, cannot be captured in the same way because it follows a non-

linear exponential decay function [134-136]. To address this, we discretized the lamp cone volume into 50 circular cross-sections along the z-axis to capture the decrease in irradiance with distance from the lamp. Each cross-section was then further divided into 29 concentric rings, with equal radial spacing, where the width (dr) at each height z was calculated as dr = (z × tan(55°))/29. The irradiance at the centerline of each ring was calculated and applied as the irradiance for that ring (I_i).

It is important to note that spatial variability in irradiance only matters in relation to the air mixing time—the rate at which pathogen-laden air becomes evenly distributed throughout a room. Pathogens in air near the lamp are inactivated by GUV most rapidly, while those outside the irradiated zone may not be inactivated at all. Thus, the mixing time, which characterizes how quickly air (and any associated pathogens) moves between zones, strongly influences GUV performance. As mentioned in Section II.VI, GUV_{222} is often assumed to be less sensitive to mixing under the premise that irradiation is distributed more uniformly throughout the space. This assumption, however, overlooks that even in "whole-room" (i.e., GUV_{222}) configurations, the irradiance values are highly variable within the room, and thus airflow patterns remain important to overall disinfection efficiency.

To evaluate the influence of imperfect air mixing on GUV_{222} disinfection performance, we modeled a simplified framework in which the position of an air parcel (and the pathogens it contains) remains fixed within each sub-volume of the irradiated region i for a length of time Δt_m (i.e., Δt_m represents a mixing delay for the room). We then approximated the survival fraction S_i of pathogens in each region i by applying a discretized form of the standard survival decay expression, based on the local GUV dose [134-136]:

$$S_i(t + \Delta t_m) = \bar{S}(t) \cdot exp\left(-k_p \cdot I_i \cdot \Delta t_m\right) \tag{11}$$

where k_p is the inactivation rate constant for a particular pathogen (m^2/J), I_i is the irradiance for each sub-volume *i,* and $\bar{S}(t)$ is the average survival fraction for the completely mixed room at the start of the timestep, set equal to 1 at t=0. In this equation, we assume that $\bar{S}(t)$ is uniform for the entire room. After the mixing delay timestep Δt_m has elapsed, pathogens are inactivated most efficiently in regions with higher irradiance, near the lamp. In the limiting case of no mixing, pathogens located in unirradiated regions would persist indefinitely. After each mixing delay timestep Δt_m, we assume the room becomes fully mixed. The average survival fraction for the room is then computed as the volume-weighted mean across all sub-volumes, which contains both irradiated and unirradiated portions of the room:

$$\bar{S}(t + \Delta t_m) = \frac{\sum_i V_i S_i(t + \Delta t_m)}{\sum_i V_i} \tag{12}$$

where V_i is the sub-volume. This value becomes the input for the next iteration of Eq. 11. As $\Delta t_m \rightarrow 0$, the solution approaches the ideal well-mixed case with no mixing delay. Larger Δt_m values lead to more pronounced deviations, particularly for pathogens with larger k_p, due to

higher survival gradients between irradiated and unirradiated regions. Simulations were conducted for 2000 iterations, with Δt_m varied between 1 and 200 s. For each simulated pathogen k_p and mixing delay Δt_m, we fit an exponential decay function to the discretized $\bar{S}(t)$ result and used least-squares regression to determine the decay constant (λ) for each $\bar{S}(t)$ result:

$$\bar{S}(t) = e^{-\lambda t} \tag{13}$$

Finally, we calculated the effective irradiance for the room from the decay constant and the k_p value:

$$I_{rm} = \lambda / k_p \tag{14}$$

This result represents the effective irradiance for the room, in its entirety, taking account both the effects of the irradiance distribution and the effect of the mixing delay timestep. From this value, we calculate the clean air delivery rate (CADR) for GUV from the effective room irradiance, inactivation rate constant, and room volume:

$$CADR_{GUV} = k_p \cdot I_{rm} \cdot V \tag{15}$$

Figure 8a and 8c shows the dependence of effective room irradiance, I_{rm}, on mixing delay (Δt_m) for selected pathogen inactivation rate constants (k_p = 1.14–14.26 cm^2 mJ^{-1}) under the 3.05 m ceiling configuration. As expected, slower air mixing time (increasing Δt_m) leads to a greater reduction in effective irradiance, particularly for pathogens with higher inactivation rate constants. When mixing is rapid ($\Delta t_m \rightarrow 0$), the same equivalent room irradiance is achieved for all k_p values. This value, I_{rm}=0.68 μW cm^{-2} for the 3.05 m ceiling and I_{rm}=0.27 μW cm^{-2} for the 2.45 m ceiling, is simply the volume-weighted average irradiance of the entire room. As mixing slows, the combined influence of the inactivation rate and the mixing delay increasingly governs the effective irradiance; in other words, pathogens with smaller inactivation rate constants are less sensitive to imperfect mixing.

Air mixing time is a critical but poorly constrained parameter in GUV disinfection modeling. In practice, mixing is governed by room geometry, ventilation strategy, supply air temperature, and occupancy-driven thermal plumes, and can vary substantially across real buildings. The most directly relevant experimental characterization comes from Um et al. (2025), who used a pulsed ethanol tracer with a network of fast-response sensors to quantify mixing in a 158 m^3 mechanically ventilated meeting room [137]. They reported full room mixing times of 3–4 minutes under high supply airflow at neutral temperature, and 7.5–9 minutes when heated supply air was provided at a lower flow rate [137]. CFD-based studies of pollutant mixing in mechanically mixed rooms similarly found mixing timescales on the order of 1–10 minutes depending on fan power, consistent with the tracer-gas measurements [138, 139]. For upper-room GUV_{254} systems, Noakes et al. (2004) demonstrated through two-zone modeling that inter-zone airflow — and by extension the rate at which pathogen-laden

air circulates through the irradiated zone — is a primary determinant of overall disinfection performance, underscoring the sensitivity of GUV efficacy to this parameter more broadly [140]. Despite this body of work, no equivalent measurements have been reported specifically for whole-room GUV_{222} configurations in classroom settings, and the mixing timescale applicable to any given installation remains highly uncertain. To span a plausible range of real-world conditions, we evaluate three representative mixing delays: Δt_m = 60, 180, and 300 s. The shortest value represents an optimistic, near-ideal mixing condition that likely exceeds what is achievable in practice but serves as an upper bound on GUV_{222} performance; the intermediate value of 180 s aligns with the better-mixed conditions reported by Um et al. (2025); and the longest value of 300 s represents slower mixing more consistent with low air change rates or thermally stratified spaces. The true mixing time in a given classroom will depend on the specific ventilation system, occupancy configuration, and season of operation, and may fall outside this range in either direction. Accordingly, the results presented here should be interpreted as bracketing plausible performance rather than as predictions for a specific installation.

Figure 8b and 8d compares the total CADR as a function of k_p for three representative mixing delays under different ventilation conditions: ASHRAE 62.1 outdoor air (OA) supplemented with three GUV_{222} units, three GUV_{222} units alone, and ASHRAE 241 achieved solely with outdoor air. For the ASHRAE 241 outdoor air case, the CADR of 624 L s^{-1} is constant because it is determined entirely by the ventilation rate. When GUV_{222} is used, the CADR increases with k_p, but eventually plateaus due to the mixing delay. The relative performance of GUV_{222} versus ASHRAE 241 OA is highly sensitive to both ceiling height and mixing time. An important implication of Figure 8 is the presence of an inactivation rate constant threshold at which clean air delivery rate from the GUV_{222} scenario exceeds the increased outdoor air rate scenario. Specifically, the intersection of the dotted curves with the red reference line occurs at approximately k_p^* = 2.3 cm^2 mJ^{-1} for the 3.05 m ceiling. This indicates that when pathogen susceptibility to 222-nm irradiation exceeds this value, GUV_{222} provides greater equivalent CADR than increased outdoor air ventilation under the modeled conditions, whereas lower values favor ventilation. At the 2.45 m ceiling, the corresponding threshold rises to approximately 7.7 cm^2 mJ^{-1} at a mixing delay of 60 s and increases further at longer mixing delays, such that at 300 s the GUV_{222} scenario fails to reach the ASHRAE 241 CADR threshold across the entire range of k_p examined.

For pathogens with high k_p values (e.g. 20.08 cm^2/mJ) and minimal room mixing delays (e.g. 60 s), the GUV_{222} scenario may provide up to approximately five times the CADR compared to the ASHRAE 241 outdoor air scenario. However, because reported k_p values for airborne pathogens vary by an order of magnitude with high uncertainty, and because the air mixing timescale in a given space is similarly difficult to characterize or predict a priori, it is not currently possible to conclude which strategy will better perform for a given pathogen or installation. This uncertainty highlights the critical need for targeted experimental research to better quantify pathogen-specific susceptibility constants and indoor air mixing characteristics under realistic airborne conditions.

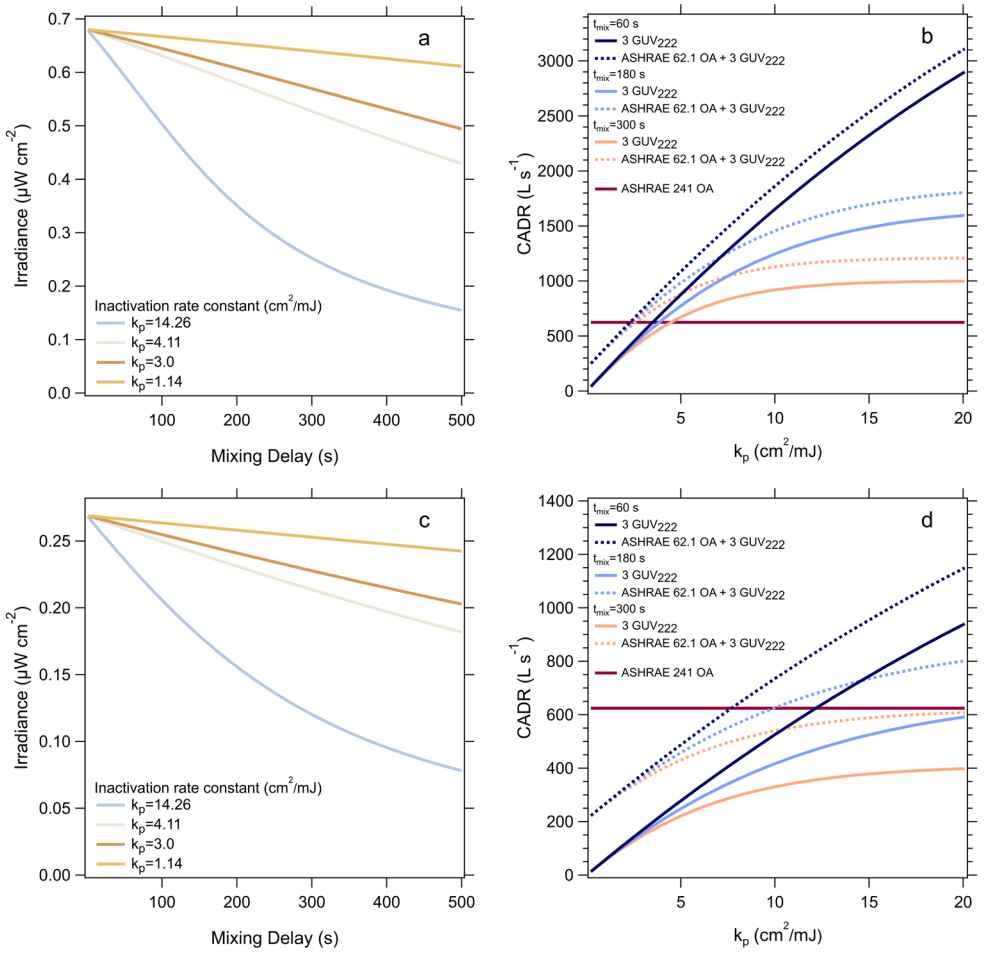

Figure 8. Effect of ceiling height on GUV_{222} performance for a 3.05 m ceiling (a, b) and a 2.45 m ceiling (c, d). (a, c) Average irradiance as a function of mixing delay for pathogens with inactivation rate constants spanning nearly an order of magnitude (k_p = 1.14–14.26 cm^2 mJ^{-1}). (b, d) CADR as a function of pathogen susceptibility k_p for three mixing delays (Δt_m = 60, 180, and 300 s) across different ventilation configurations: three GUV_{222} units, ASHRAE 62.1 outdoor air with GUV_{222}, and ASHRAE 241 outdoor air alone.

Table 7 and Table 8 summarize literature-reported susceptibility constants for a range of viral and bacterial pathogens in air, along with the corresponding effective room irradiance values predicted by our model for mixing delays of 60 s, 180 s, and 300 s, and the resulting CADR values for the 3.05 ceiling scenario (Table 7) and 2.45 m ceiling scenario (Table 8). Across both ceiling heights, the qualitative pattern is consistent; for pathogens with moderate to high UV susceptibility, the GUV_{222} CADR contribution (shown in the table) combined with the ASHRAE 62.1 minimum outside air requirement delivers CADR values that meet or exceed the 624 L s^{-1} provided by ASHRAE 241 outdoor air alone. The advantage of GUV_{222} increases with higher ceiling heights and shorter mixing delays. For pathogens with low susceptibility, the GUV_{222} scenario falls below the ASHRAE 241 CADR benchmark regardless of mixing delay, delivering less equivalent clean air than the outdoor-air-only strategy. The magnitude of the GUV_{222} advantage is substantially reduced at the lower ceiling height. At 3.05 m, CADR values for highly susceptible pathogens range from roughly 1.5 to nearly 5 times the ASHRAE 241 benchmark at 60 s mixing delay, whereas at 2.45 m the corresponding range is approximately 1 to 1.7 times, reflecting the reduced lamp output required to comply with photobiological safety limits at that ceiling height.

For context, these modeled CADR values are broadly consistent with those reported by Abboushi et al. (2025) [92], who estimated $CADR_{GUV}$ from measured average irradiance under ideal mixing assumptions. For example, in a school classroom (40 m^2, 3.23 m ceiling height) equipped with a single GUV_{222} unit, they reported a mean fluence rate of 0.3 μW cm^{-2}, corresponding to CADRs of 307 and 373 L s^{-1} for coronaviruses with k_p values of 7.7 and 9.35 cm^2 mJ^{-1}, respectively. Similarly, for bacteriophage MS2 (k_p = 0.78 and 2.45 cm^2 mJ^{-1}), the estimated CADRs were 31 and 98 L s^{-1}. These values are not directly comparable to our results given differences in room size, number of lamps, ceiling height, and the assumption of ideal mixing; however, the order-of-magnitude agreement in CADR across similar k_p ranges lends confidence to the overall modeling framework.

Table 7. CADR for 3.05 m ceiling scenario for example Pathogens under three mixing delays (60, 180, and 300 s).

Pathogen	**k_p (cm^2 mJ^{-1}) (low estimate)**	**k_p (cm^2 mJ^{-1}) (high estimate)**	**Effective I_{rm} (μW cm^{-2}) (low k_p estimate)**	**Effective I_{rm} (μW cm^{-2}) (high k_p estimate)**	**CADR for GUV_{222}**
Mixing delay time = 60 s					
Coronavirus	1.14[a]	14.26 [a]	0.6723	0.5753	208 – 2232 L s^{-1}
Influenza	1.8[b]		0.6677		327 L s^{-1}
Bacteriophage P22	3[c]	17.14[c]	0.6592	0.5533	538 – 2580 L s^{-1}
Bacteriophage MS2	0.22[d]	5.75 [d]	0.6787	0.6393	41 – 1000 L s^{-1}
Bacteriophage Phi6	20.08[e]		0.531		2900 L s^{-1}
Mixing delay time = 180 s					
Coronavirus	1.14[a]	14.26 [a]	0.6562	0.3769	203 – 1462 L s^{-1}
Influenza	1.8[b]		0.6419		314 L s^{-1}
Bacteriophage P22	3[c]	17.14[c]	0.6152	0.3313	502 – 1544 L s^{-1}
Bacteriophage MS2	0.22[d]	5.75 [d]	0.6756	0.5525	40 – 864 L s^{-1}
Bacteriophage Phi6	20.08[e]		0.2923		1596 L s^{-1}
Mixing delay time = 300 s					
Coronavirus	1.14[a]	14.26 [a]	0.6397	0.2526	198 – 980 L s^{-1}
Influenza	1.8[b]		0.6152		301 L s^{-1}
Bacteriophage P22	3[c]	17.14[c]	0.5697	0.2131	465 – 993 L s^{-1}
Bacteriophage MS2	0.22[d]	5.75 [d]	-0.6726	0.4672	40 – 731 L s^{-1}
Bacteriophage Phi6	20.08[e]		0.1829		999 L s^{-1}

[a] [26, 97], [b] [25], [c] [57, 94], [d] [94, 141], [e] [100]

Table 8. CADR calculations for 2.45 m scenario for example pathogens under three mixing delays (60, 180, and 300 s).

Pathogen	**k_p (cm^2 mJ^{-1}) (low estimate)**	**k_p (cm^2 mJ^{-1}) (high estimate)**	**Effective I_{rm} (μW cm^{-2}) (low k_p estimate)**	**Effective I_{rm} (μW cm^{-2}) (high k_p estimate)**	**CADR for GUV_{222}**
Mixing delay time = 60 s					
Coronavirus	1.14[a]	14.26 [a]	0.2657	0.2297	66 – 714 L s^{-1}
Influenza	1.8[b]		0.2638		104 L s^{-1}
Bacteriophage P22	3[c]	17.14[c]	0.2604	0.2222	170 – 830 L s^{-1}
Bacteriophage MS2	0.22[d]	5.75 [d]	0.2683	0.2527	13 – 317 L s^{-1}
Bacteriophage Phi6	20.08[e]		0.2148		940 L s^{-1}
Mixing delay time = 180 s					
Coronavirus	1.14[a]	14.26 [a]	0.2592	0.1647	64 – 512 L s^{-1}
Influenza	1.8[b]		0.2537		100 L s^{-1}
Bacteriophage P22	3[c]	17.14[c]	0.2438	0.1492	159 – 557 L s^{-1}
Bacteriophage MS2	0.22[d]	5.75 [d]	0.267	0.2219	13 – 278 L s^{-1}
Bacteriophage Phi6	20.08[e]		0.1352		592 L s^{-1}
Mixing delay time = 300 s					
Coronavirus	1.14[a]	14.26 [a]	0.2529	0.1202	63– 374 L s^{-1}
Influenza	1.8[b]		0.2438		96 L s^{-1}
Bacteriophage P22	3[c]	17.14[c]	0.2277	0.1041	149 – 389 L s^{-1}
Bacteriophage MS2	0.22[d]	5.75 [d]	0.2658	0.194	13 – 243 L s^{-1}
Bacteriophage Phi6	20.08[e]		0.091		398 L s^{-1}

[a] [26, 97], [b] [25], [c] [57, 94], [d] [94, 141], [e] [100]

Overall, these results demonstrate that reducing ceiling height requires reducing the lamp power output to meet skin and eye safety requirements. While the qualitative relationships between CADR, pathogen susceptibility, and mixing are preserved, this reduction is reflected in a substantial upward shift in the critical susceptibility threshold k_p^*: from ~2.3 cm^2 mJ^{-1} at the 3.05 m ceiling to 7.7 cm^2 mJ^{-1} (Δt_m = 60 s) and 10 cm^2 mJ^{-1} (Δt_m = 180 s) at the 2.45 m ceiling height. GUV_{222} systems therefore deliver greater advantages over outdoor-air ventilation in spaces with higher ceilings, where photobiological safety constraints permit higher irradiance levels and a larger irradiated volume. Because both the susceptibility of the target pathogen and the mixing characteristics of the space are often unknown or highly variable, the real-world disinfection performance of GUV_{222} devices remains difficult to predict for a specific installation.

VII. Ozone emission test standards for GUV_{222} systems

VII.I UL 867 and UL 2998

California Assembly Bill 2276 (2006, Pavley) directed the State to regulate the amount of ozone emitted from indoor air cleaners for public health. CARB manages and enforces this regulation [142], which currently limits emissions to no more than 50 ppb ozone. Devices are certified through testing under Underwriters Laboratories (UL) Standard 867 – Electrostatic Air Cleaners [143]. In this procedure, the air cleaner is installed in a test chamber of volume 26.9 to 31.1 m^3 with an ozone decay rate configured to be 1.33 h^{-1}. The device is then operated continuously for up to 24 hours (an 8-hour test is permissible if ozone levels are not increasing), while ozone concentration two inches from the device is monitored. To pass, the measured concentration must remain below 50 ppb throughout the test period.

UL Standard 2998 –Environmental Claim Validation Procedure for Zero Ozone Emissions from Air Cleaners specifies the same ozone test method as UL 867, with a maximum average of 5 ppb over a 5 minute period [144]. Air cleaners validated to UL 2998 must be tested at least every three years, with surveillance audits occurring in non-testing years to ensure continued compliance and evaluate changes in the air cleaner materials and/or manufacturing that may alter ozone emissions. UL 2998 uses the UL 867 test method and does not directly measure ozone emission rate; it is a measure of the maximum ozone concentration near the outlet of the air cleaner. UL 2998 does not ensure "Zero Ozone Emissions from Air Cleaners" as the title of the standard implies, as some ozone production is permissible under the test criteria.

VII.II Interpreting Concentration-based Results from UL 867 and UL 2998

The practice of reporting UL 867 test results in terms of ozone concentration can be misleading if interpreted as representative of the increase that would occur in a building under real-world conditions. In practice, the ozone concentration indoors depends not only on the device's emission rate but also on the building air volume and removal processes such as deposition and ventilation. As a result, a test result of 50 ppb under UL 867 or 5 ppb under UL 2998 does not directly translate to the concentration change that would occur when the device operates in an actual building.

A mass-balance model for the UL 867 test chamber can be used to relate the measured concentration from the test protocol to a mass-based emission rate. For a well-mixed chamber and negligible background ozone concentration, a mass balance of the chamber takes the form of Equation 16:

$$\frac{dc}{dt} = \frac{E}{V} - kC \tag{16}$$

where C is the ozone concentration in chamber, E is ozone emission rate of the source (i.e., air cleaner), V is volume of the chamber, and k is the first-order ozone decay rate due to removal processes, which is defined by UL 867 to be 1.33 h^{-1}. By the end of the test period,

we can assume that the ozone concentration is at steady-state and not changing with time, such that $\frac{dC}{dt} = 0$. We then rearrange Equation 16 to be:

$$E = \frac{1.33}{h} \times C \times V \tag{17}$$

Although UL 867 allows a small range of chamber sizes, using the largest permitted chamber (31.1 m^3) yields the highest allowable device emission rate for a unit that passes at the maximum concentration of 50 ppb:

$$E \leq (31.1\ m^3)\left(\frac{1.33}{h}\right)(50\ ppb)\ =\ 2{,}068\ \frac{ppb}{h} \tag{18}$$

Applying the ideal gas law at 25 °C and the molecular weight of ozone (48 g mol^{-1}), 1 ppb of ozone corresponds to a mass density of 1.96 µg m^{-3}. This value can then be used to calculate the maximum mass-based emission rate for the device:

$$E \leq 2{,}068\ \frac{ppb}{h}\left(\frac{\frac{1.96\ \mu g}{m^3}}{1\ ppb}\right) = \frac{4{,}054\ \mu g}{hr} \tag{19}$$

Thus, although UL 867 does not directly measure emission rates, we can reasonably conclude that a passing device could generate up to approximately 4 mg h^{-1}. Similarly, repeating the calculation for the 5 ppb allowable concentration under UL 2998 shows that a passing device could generate up to approximately 0.4 mg h^{-1}. These test standards provide context for allowable ozone emission levels relative to regulatory limits and to the emission of the example GUV_{222} lamp modeled in Section V.II. Our model estimated ozone production of 0.88 mg h^{-1} for the lamp mounted 3.05 m from the floor, indicating that the lamp would pass UL 867 but not UL 2998.

VII.III Additional Challenges of Testing GUV Lamps under UL 867 and UL 2998

UL 867, and UL 2998 were originally developed for testing electrostatic air cleaners; the standards were not designed with GUV_{222} lamps in mind. As described in Section V.II, the ozone generation rate depends on the lamp's irradiance inside the chamber, which decreases with distance from the source. If the chamber walls interfere with the irradiance field, ozone generation will be reduced. For a ceiling-mounted lamp, the distance from the lamp center to the chamber walls and floor is therefore an important factor.

UL 867 specifies that the test chamber must have a minimum width of 2.4 m and a maximum height of 3.0 m, but it does not define a minimum height. Because testing of GUV_{222} lamps was not anticipated when the standard was written, it provides no guidance on lamp mounting or installation within the chamber. As a result, UL 867 omits important criteria needed to ensure repeatable and accurate testing of GUV_{222} lamps. Assuming an implementer applies UL 867 using a reasonable ceiling height of 2.45 m, a chamber with a volume of 31.1 m^3 would correspond to square floor dimensions of 3.56 m per side. A

potential concern is that part of the lamp's emission cone would be truncated by the chamber walls (Figure 9, left). However, we estimate that truncation by chamber walls for the Ushio B1 lamp (modeled in Section V.II) would reduce ozone emissions by less than 3% compared to the full cone, which is consistent with the fact that the portion of irradiance cut off occurs far from the source. Therefore, provided that a chamber of reasonable ceiling height is used and lamps are mounted to minimize wall interference, applying UL 867 should yield reasonably accurate results on a mass emission rate basis.

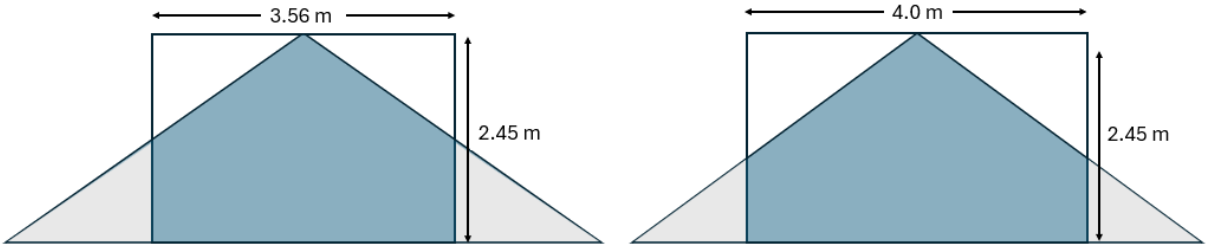

Figure 9. Side view of example UL 867 chamber (width of 2.56 m) illustrating chamber walls interfering with projection of illuminance cone with 55° half angle (left). ASTM Standard D8625 requires a minimum width of 4.0, reducing interference of the GUV_{222} source and the chamber walls (right).

VII.IV ASTM Standard D8625 – Standard Test Method for Chemical Assessment of Air Cleaning Technologies

Recently published ASTM Standard D8625 – Standard Test Method for Chemical Assessment of Air Cleaning Technologies evaluates the ability on an air cleaner to remove injected challenge chemicals from the air [145]. The test method also quantifies chemical byproducts generated by the air cleaner, including formaldehyde, ozone, nitrogen oxides, and ultrafine particles. While the test method is designed to evaluate more than just ozone, it can also be conducted solely to assess ozone generation. ASTM D6825 addresses shortcomings of UL 867 for testing GUV_{222} lamps by specifying a minimum chamber height of 2.25 m and requiring that lamps be mounted on the ceiling at the chamber's center with UV emissions directed downward. The standard also mandates that the emitted UV is unobstructed by chamber walls or other objects for at least 2 m, effectively requiring a chamber width and length of at least 4 m (Figure 9, right). For this slightly larger chamber, we estimate that truncation by chamber walls for the Ushio B1 lamp (modeled in Section V.II) would reduce ozone emissions by less than 1.4% compared to the full cone. Additionally, the ASTM 8625 measurement and analysis method applies a mass-balance model to calculate ozone emissions in mass-based units (mg/hr) rather than concentrations (ppb), allowing chamber sizes up to 125 m^3 to be used while yielding consistent results. Reporting emissions on a mass basis also prevents misinterpretation of concentration results as directly representative of conditions in actual buildings.

VII.V UL 867 – Ozone Emissions Task Group

In May 2025, a task group was formed to revise UL 867 to improve ozone emissions testing and reporting and to accommodate testing of GUV_{222} lamps. The well-supported group, led by Standards Project Manager Michael Niedermayer, includes members from universities, industry, government agencies, and non-profit organizations. More information on the current status of the task group can be obtained by contacting UL [146].

VIII. Conclusions

Our analysis evaluated the ozone-related impacts and air-disinfection performance of GUV_{222} relative to increasing outdoor air ventilation to meet ASHRAE Standard 241 for an example classroom application. The modeled GUV_{222} scenario intentionally pushes toward the upper end of permissible GUV irradiance for skin and eye safety to characterize the highest realistic levels of ozone generation and disinfection effectiveness.

Our modeling demonstrates that, under typical ambient ozone conditions in California, supplementing ASHRAE Standard 62.1 outdoor-air ventilation with GUV_{222} yields lower indoor ozone concentrations than relying solely on higher outdoor-air ventilation rates to achieve the required equivalent clean airflow. Because outdoor ozone is the dominant source of indoor ozone in most buildings, increasing outdoor-air ventilation introduces substantially more ozone indoors than the ozone generation associated with GUV_{222} systems operating within the bounds of current skin and eye safety standards. Only when average outdoor ozone concentrations fall below 10.7 ppb (for the 3.05 m ceiling) or 6.8 ppb (for the 2.45 m ceiling)—substantially lower than typical background levels—would the outdoor-air strategy result in lower indoor ozone than the GUV_{222} scenario.

By discretizing the irradiance field and applying pathogen-specific inactivation rate constants, we determined that GUV_{222} can deliver ECA values comparable or higher than those associated with increased outdoor-air ventilation, particularly for pathogens with moderate to high UV susceptibility. For air disinfection, the modeled GUV_{222} scenario met or exceeded ASHRAE 241 for pathogen inactivation constants (k_p) greater than 2.3 cm^2 mJ^{-1} for the 3.05 m ceiling scenario and 7.7 cm^2 mJ^{-1} for the 2.45 m ceiling scenario. For pathogens with high k_p values (e.g. 20.08 cm^2/mJ) and minimal room mixing delays (e.g. 60 s), the GUV_{222} scenario may provide up to approximately five times the CADR compared to the ASHRAE 241 outdoor air scenario. However, because reported k_p values for airborne pathogens vary by an order of magnitude with high uncertainty, and because the air mixing timescale in a given space is similarly difficult to characterize or predict a priori, it is not currently possible to conclude which strategy will dominate for a given pathogen or installation. This uncertainty highlights the critical need for targeted experimental research to better quantify both pathogen-specific susceptibility constants and indoor air mixing characteristics under realistic airborne conditions.

Taken together, the results indicate that integrating GUV_{222} with standard ventilation has potential for achieving infection-control goals while limiting indoor ozone exposure. This

conclusion, however, applies specifically to ozone; a comprehensive assessment would also consider ozone-reaction byproducts, energy implications of increased outdoor-air ventilation and operation of GUV_{222}, and the performance of filtration-based alternatives, which can provide clean air without generating ozone. Additionally, the conclusions are limited to the analyzed scenario; additional simulations are needed to draw more general conclusions for a variety of applications. The framework outlined and applied in this paper is a useful tool that can be expanded to consider additional scenarios.

References

1. Seker, H., et al., *UV-C-induced DNA damage leads to p53-dependent nuclear trafficking of PML*. Oncogene, 2003. **22**(11): p. 1620-1628.
2. Kowalski, W., *Ultraviolet germicidal irradiation handbook: UVGI for air and surface disinfection*. 2010: Springer science & business media.
3. Blatchley Iii, E.R., et al., *Far UV-C radiation: An emerging tool for pandemic control.* Critical Reviews in Environmental Science and Technology, 2023. **53**(6): p. 733-753.
4. Pfeifer, G.P., Y.-H. You, and A. Besaratinia, *Mutations induced by ultraviolet light.* Mutation Research/Fundamental and Molecular Mechanisms of Mutagenesis, 2005. **571**(1): p. 19-31.
5. Vink, A.A., et al., *Induction, repair and accumulation of thymin dimers in the skin of UV-B-irradiated hairless mice*. Carcinogenesis, 1991. **12**(5): p. 861-864.
6. Pfeifer, G.P. and A. Besaratinia, *UV wavelength-dependent DNA damage and human non-melanoma and melanoma skin cancer*. Photochemical & Photobiological Sciences, 2012. **11**(1): p. 90-97.
7. Wells, W.F., *Air Disinfection in Day Schools*. American Journal of Public Health and the Nations Health, 1943. **33**(12): p. 1436-1443.
8. Görlitz, M., et al., *Assessing the safety of new germicidal far-UVC technologies.* Photochem Photobiol, 2024. **100**(3): p. 501-520.
9. Newsletter, W.E. *THE DEATH RAY THAT GUARDS LIFE*. 1943; Available from: *https://archive.warplane.com/omeka/s/archive/item/20985*.
10. Jimenez, J.L., et al., *What were the historical reasons for the resistance to recognizing airborne transmission during the COVID-19 pandemic?* Indoor Air, 2022. **32**(8): p. e13070.
11. Riley, R.L., *The contagiosity of tuberculosis.* Schweiz Med Wochenschr, 1983. **113**(3): p. 75-9.
12. Daniel, T.M., *The history of tuberculosis.* Respiratory Medicine, 2006. **100**(11): p. 1862-1870.
13. First, M.W., et al., *Monitoring human exposures to upper-room germicidal ultraviolet irradiation.* Journal of occupational and environmental hygiene, 2005. **2**(5): p. 285-292.
14. Brickner, P.W., et al., *The application of ultraviolet germicidal irradiation to control transmission of airborne disease: bioterrorism countermeasure*. Public Health Reports, 2003.
15. Nunayon, S.S., H. Zhang, and A.C.K. Lai, *Comparison of disinfection performance of UVC-LED and conventional upper-room UVGI systems.* Indoor Air, 2020. **30**(1): p. 180-191.
16. Reed, N.G., *The history of ultraviolet germicidal irradiation for air disinfection.* Public Health Rep, 2010. **125**(1): p. 15-27.
17. Johnson, A., *Scientific Responses to Concerns With Use of UV-C as an Indoor Disinfection Process*. 2024, Purdue University.
18. Bang, J.-I., et al., *Sterilization effectiveness of in-duct ultraviolet germicidal irradiation system in liquid desiccant and indirect/direct evaporative cooling-assisted 100% outdoor air system.* Building and Environment, 2020. **186**: p. 107350.
19. Kujundzic, E., M. Hernandez, and S.L. Miller, *Ultraviolet germicidal irradiation inactivation of airborne fungal spores and bacteria in upper-room air and HVAC in-duct configurations.* Journal of Environmental Engineering and Science, 2007. **6**(1): p. 1-9.
20. Narita, K., et al., *Chronic irradiation with 222-nm UVC light induces neither DNA damage nor epidermal lesions in mouse skin, even at high doses.* PLoS One, 2018. **13**(7): p. e0201259.
21. Buonanno, M., et al., *Germicidal Efficacy and Mammalian Skin Safety of 222-nm UV Light.* Radiat Res, 2017. **187**(4): p. 483-491.

22. Buonanno, M., et al., *207-nm UV Light-A Promising Tool for Safe Low-Cost Reduction of Surgical Site Infections. II: In-Vivo Safety Studies*. PLoS One, 2016. **11**(6): p. e0138418.
23. Buonanno, M., D. Welch, and D.J. Brenner, *Exposure of Human Skin Models to KrCl Excimer Lamps: The Impact of Optical Filtering*. Photochemistry and Photobiology, 2021. **97**(3): p. 517-523.
24. Seyedi, S., et al., *Field Study and Evaluation of KrCl* Far UV-C Device Capability for Inactivation of Phi6 Bacteriophage*. Photochemistry and Photobiology, 2023. **99**(5): p. 1293-1298.
25. Welch, D., et al., *Far-UVC light: A new tool to control the spread of airborne-mediated microbial diseases*. Scientific Reports, 2018. **8**(1): p. 2752.
26. Buonanno, M., et al., *Far-UVC light (222 nm) efficiently and safely inactivates airborne human coronaviruses*. Scientific Reports, 2020. **10**(1): p. 10285.
27. Fukui, T., et al., *Exploratory clinical trial on the safety and bactericidal effect of 222-nm ultraviolet C irradiation in healthy humans*. PLoS One, 2020. **15**(8): p. e0235948.
28. Eadie, E., et al., *Extreme Exposure to Filtered Far-UVC: A Case Study(†)*. Photochem Photobiol, 2021. **97**(3): p. 527-531.
29. Hickerson, R., et al., *Minimal, superficial DNA damage in human skin from filtered far-ultraviolet C*. British Journal of Dermatology, 2021. **184**(6): p. 1197-1199.
30. Ong, Q., et al., *222-Nanometer Far-UVC Exposure Results in DNA Damage and Transcriptional Changes to Mammalian Cells*. International Journal of Molecular Sciences, 2022. **23**(16): p. 9112.
31. Eadie, E., et al., *Far-UVC: The impact of optical filters on real-world deployment*. Photochem Photobiol, 2025. **101**(2): p. 270-274.
32. Sharma, R. *Far-UVC 222 nm Upper-Air Devices Market*. Available from: *https://dataintelo.com/report/far-uvc-222-nm-upper-air-devices-market*.
33. Sliney, D.H. and B.E. Stuck, *A Need to Revise Human Exposure Limits for Ultraviolet UV-C Radiation*. Photochemistry and Photobiology, 2021. **97**(3): p. 485-492.
34. Biosecurity, B., *Blueprint for Far-UVC*. 2025.
35. *ANSI/CAN/UL 8802*. 2024.
36. Claus, H., *Expected ACGIH eye exposure when using 222 nm ceiling mounted sources*. Optical Radiation News, 2022.
37. Weschler, C.J., *Ozone in indoor environments: concentration and chemistry*. 2000.
38. Nazaroff, W.W. and C.J. Weschler, *Indoor ozone: Concentrations and influencing factors*. Indoor Air, 2022. **32**(1): p. e12942.
39. Poppendieck, D., et al., *Ozone reactions with indoor materials during building disinfection*. Atmospheric Environment, 2007. **41**(15): p. 3166-3176.
40. Morrison, G.C. and W.W. Nazaroff, *The rate of ozone uptake on carpet: mathematical modeling*. Atmospheric Environment, 2002. **36**(11): p. 1749-1756.
41. Wells, J.R., *Gas-Phase Chemistry of α-Terpineol with Ozone and OH Radical: Rate Constants and Products*. Environmental Science & Technology, 2005. **39**(18): p. 6937-6943.
42. Weschler, C.J. and H.C. Shields, *Indoor ozone/terpene reactions as a source of indoor particles*. Atmospheric Environment, 1999. **33**(15): p. 2301-2312.
43. Lee, K., et al., *Ozone decay rates in residences*. Journal of the Air & Waste Management Association, 1999. **49**(10): p. 1238-1244.
44. Seinfeld, J.H. and S.N. Pandis, *Atmospheric chemistry and physics: from air pollution to climate change*. 2016: John Wiley & Sons.

45. Mauderly, J.L. and J.C. Chow, *Health Effects of Organic Aerosols.* Inhalation Toxicology, 2008. **20**(3): p. 257-288.

46. 241, S., *Control of Infectious Aerosols.* 2023.

47. CDC, *Environmental Control for Tuberculosis: Basic Upper-Room Ultraviolet Germicidal Irradiation Guidelines for Healthcare Settings.* 2009.

48. Kowalski, W., *UVGI Guidelines and Standards*, in *Ultraviolet Germicidal Irradiation Handbook: UVGI for Air and Surface Disinfection*, W. Kowalski, Editor. 2009, Springer Berlin Heidelberg: Berlin, Heidelberg. p. 255-286.

49. Society, I.E., *Recommended Practice: Ultraviolet Germicidal Irradiation (UVGI).* 2021.

50. Cappa, C., *Air Pollutant Emissions and Possible Health Effects Associated with Electronic Air Cleaners.* 2023.

51. Collins, D.B. and D.K. Farmer, *Unintended Consequences of Air Cleaning Chemistry.* Environmental Science & Technology, 2021. **55**(18): p. 12172-12179.

52. Siegel, J.A., *Primary and secondary consequences of indoor air cleaners.* Indoor Air, 2016. **26**(1): p. 88-96.

53. Pistochini, T., C. Mande, and S. Chakraborty, *Modeling impacts of ventilation and filtration methods on energy use and airborne disease transmission in classrooms.* Journal of Building Engineering, 2022. **57**: p. 104840.

54. Björn, L.O. and A.H. Teramura, *Simulation of daylight ultraviolet radiation and effects of ozone depletion*, in *Environmental UV photobiology*. 1993, Springer. p. 41-71.

55. Li, P., et al., *Is line-source modeling suitable for ultraviolet light application in an air cleaner duct?* Frontiers in Built Environment, 2024. **10**: p. 1325267.

56. Sasges, M., R. Jim, and F. and Daynouri, *Ultraviolet Lamp Output Measurement: A Concise Derivation of the Keitz Equation.* Ozone: Science & Engineering, 2012. **34**(4): p. 306-309.

57. Zhang, H. and A.C.K. Lai, *Evaluation of Single-Pass Disinfection Performance of Far-UVC Light on Airborne Microorganisms in Duct Flows.* Environmental Science & Technology, 2022. **56**(24): p. 17849-17857.

58. Link, M.F., et al., *Ozone Generation from a Germicidal Ultraviolet Lamp with Peak Emission at 222 nm.* Environmental Science & Technology Letters, 2023. **10**(8): p. 675-679.

59. Claus, H. and C.C. Cooksey. *Reflectance measurements of building materials in the far UVC (222 nm) wavelength range*. in *UV and Higher Energy Photonics: From Materials to Applications 2022*. 2022. SPIE.

60. Ma, B., et al., *Reflection of UVC wavelengths from common materials during surface UV disinfection: Assessment of human UV exposure and ozone generation.* Science of The Total Environment, 2023. **869**: p. 161848.

61. Chapman, S., *A theory of upper-atmospheric ozone.* Mem. Roy. Meteor. Soc., 1930. **3**: p. 103-125.

62. Peng, Z., et al., *Significant Production of Ozone from Germicidal UV Lights at 222 nm.* Environmental Science & Technology Letters, 2023. **10**(8): p. 668-674.

63. Link, M.F., et al., *Ozone generation and chemistry from 222 nm germicidal ultraviolet light in a fragrant restroom.* Environmental Science: Processes & Impacts, 2024. **26**(6): p. 1090-1106.

64. Narouei, F., et al., *Effects of Germicidal Far-UVC on Indoor Air Quality in a Conference Room.* 2024.

65. Paulson, S.E., R.C. Flagan, and J.H. Seinfeld, *Atmospheric photooxidation of isoprene part II: The ozone-isoprene reaction.* International Journal of Chemical Kinetics, 1992. **24**(1): p. 103-125.

66. Paulson, S.E. and J. Seinfeld, *Atmospheric Photochemical Oxidation of 1-Octene: OH, O3, and O(3P) Reactions.* Environmental Science & Technology, 1992. **26**(6): p. 1165-1173.

67. Barber, V.P., et al., *Indoor Air Quality Implications of Germicidal 222 nm Light*. Environmental Science & Technology, 2023. **57**(42): p. 15990-15998.

68. Jenks, O.J., et al., *Effects of 222 nm Germicidal Ultraviolet Light on Aerosol and VOC Formation from Limonene*. ACS ES&T Air, 2024. **1**(7): p. 725-733.

69. Young, C.J., et al., *Illuminating the dark side of indoor oxidants*. Environ Sci Process Impacts, 2019. **21**(8): p. 1229-1239.

70. Goss, M.B. and J.H. Kroll, *Organic aerosol formation from 222 nm germicidal light: ozone-initiated vs. non-ozone pathways*. Environmental Science: Processes & Impacts, 2025.

71. Tahsini, N., et al., *Mitigation of Indoor Ozone and Secondary Products from 222 nm Germicidal UV Using Commercial Air Cleaners*. 2025.

72. Carter, T.J., et al., *The Impact of UVC Light on Indoor Air Chemistry: A Modeling Study*. Environmental Science & Technology, 2025.

73. Rim, D., et al., *Ozone reaction with human surfaces: Influences of surface reaction probability and indoor air flow condition*. Building and Environment, 2018. **130**: p. 40-48.

74. Wisthaler, A. and C.J. Weschler, *Reactions of ozone with human skin lipids: sources of carbonyls, dicarbonyls, and hydroxycarbonyls in indoor air*. Proceedings of the National Academy of Sciences, 2010. **107**(15): p. 6568-6575.

75. Yang, S., K. Gao, and X. Yang, *Volatile organic compounds (VOCs) formation due to interactions between ozone and skin-oiled clothing: Measurements by extraction-analysis-reaction method*. Building and Environment, 2016. **103**: p. 146-154.

76. Zhou, S., M.W. Forbes, and J.P.D. Abbatt, *Kinetics and Products from Heterogeneous Oxidation of Squalene with Ozone*. Environmental Science & Technology, 2016. **50**(21): p. 11688-11697.

77. Yang, S., et al., *Ozone Initiates Human-Derived Emission of Nanocluster Aerosols*. Environmental Science & Technology, 2021. **55**(21): p. 14536-14545.

78. Peng, Z., S.L. Miller, and J.L. Jimenez, *Model Evaluation of Secondary Chemistry due to Disinfection of Indoor Air with Germicidal Ultraviolet Lamps*. Environmental Science & Technology Letters, 2023. **10**(1): p. 6-13.

79. Claus, H., *Ozone Generation by Ultraviolet Lamps*. Photochemistry and Photobiology, 2021. **97**(3): p. 471-476.

80. Huang, Y., et al., *Physical parameters effect on ozone-initiated formation of indoor secondary organic aerosols with emissions from cleaning products*. Journal of Hazardous Materials, 2011. **192**(3): p. 1787-1794.

81. Rai, A.C., et al., *Ozone reaction with clothing and its initiated particle generation in an environmental chamber*. Atmospheric Environment, 2013. **77**: p. 885-892.

82. Ausloos, P. and S. Lias, *Photochemistry in the far ultraviolet*. Annual review of physical chemistry, 1971. **22**(1): p. 85-107.

83. Xu, J. and C.-H. Huang, *Enhanced Direct Photolysis of Organic Micropollutants by Far-UVC Light at 222 nm from KrCl* Excilamps*. Environmental Science & Technology Letters, 2023. **10**(6): p. 543-548.

84. Lytle, C.D. and J.-L. Sagripanti, *Predicted Inactivation of Viruses of Relevance to Biodefense by Solar Radiation*. Journal of Virology, 2005. **79**(22): p. 14244-14252.

85. Pendyala, B., et al., *Genomic Modeling as an Approach to Identify Surrogates for Use in Experimental Validation of SARS-CoV-2 and HuNoV Inactivation by UV-C Treatment*. Front Microbiol, 2020. **11**: p. 572331.

86. Rockey, N.C., et al., *Predictive Modeling of Virus Inactivation by UV*. Environmental Science & Technology, 2021. **55**(5): p. 3322-3332.

87. DayIII, R.S., *CELLULAR REACTIVATION OF ULTRAVIOLET-IRRADIATED HUMAN ADENOVIRUS 2 IN NORMAL AND XERODERMA PIGMENTOSUM FIBROBLASTS.* Photochemistry and Photobiology, 1974. **19**(1): p. 9-13.
88. Harm, W., *Gene-controlled reactivation of ultraviolet-inactivated bacteriophage*. 1961. p. 69–77 pp.
89. Boszko, I.P. and A.J. Rainbow, *Removal of UV photoproducts from an adenovirus-encoded reporter gene following infection of unirradiated and UV-irradiated human fibroblasts.* Somat Cell Mol Genet, 1999. **25**(5-6): p. 301-15.
90. Leeson, R. *Viral Vectors 101: What is a Virus (and a Viral Vector)?* 2023; Available from: *https://blog.addgene.org/viral-vectors-101-what-is-a-virus-and-a-viral-vector*.
91. French, A.J., et al., *Environmental Stability of Enveloped Viruses Is Impacted by Initial Volume and Evaporation Kinetics of Droplets.* mBio, 2023. **14**(2): p. e03452-22.
92. Abboushi, B., et al., *GUV Installations Demonstrate Effectiveness and Exposure Safety in Field Settings.* Environmental Science & Technology, 2025. **59**(17): p. 8640-8650.
93. Katherine Ratliff, L.O., Worth Calfee, John Archer, *Impact of Test Methods on Far-UVC Performance Against Bioaerosols*. 2023.
94. Lu, Y.H., et al., *Evaluating the Performance of UV Disinfection across the 222–365 nm Spectrum against Aerosolized Bacteria and Viruses.* Environmental Science & Technology, 2024. **58**(16): p. 6868-6877.
95. Kitagawa, H., *Inactivation of airborne SARS-CoV-2 by 222 nm far-UVC irradiation*. 2023.
96. Buchan, A.G., et al., *Improved estimates of 222 nm far-UVC susceptibility for aerosolized human coronavirus via a validated high-fidelity coupled radiation-CFD code.* Scientific Reports, 2021. **11**(1): p. 19930.
97. Lu, Y.H., et al., *Wavelength-specific inactivation mechanisms and efficacies of germicidal UVC for airborne human coronavirus.* Journal of Hazardous Materials, 2025. **484**: p. 136666.
98. Buonanno, M., et al., *222 nm far-UVC light markedly reduces the level of infectious airborne virus in an occupied room.* Scientific Reports, 2024. **14**(1): p. 6722.
99. Xia, T., et al., *Temporal and spatial far-ultraviolet disinfection of exhaled bioaerosols in a mechanically ventilated space.* Journal of Hazardous Materials, 2022. **436**: p. 129241.
100. Eadie, E., et al., *Far-UVC (222 nm) efficiently inactivates an airborne pathogen in a room-sized chamber.* Scientific Reports, 2022. **12**(1): p. 4373.
101. Cao, G., et al., *A review of the performance of different ventilation and airflow distribution systems in buildings.* Building and environment, 2014. **73**: p. 171-186.
102. Fisk, W.J., et al., *Air change effectiveness and pollutant removal efficiency during adverse mixing conditions.* Indoor Air, 1997. **7**(1): p. 55-63.
103. Beggs, C.B. and P. Sleigh, *A quantitative method for evaluating the germicidal effect of upper room UV fields.* Journal of Aerosol Science, 2002. **33**(12): p. 1681-1699.
104. Park, S., et al., *Effect of ventilation strategy on performance of upper-room ultraviolet germicidal irradiation (UVGI) system in a learning environment.* Science of the Total Environment, 2023. **899**: p. 165454.
105. Klepeis, N.E., et al., *The National Human Activity Pattern Survey (NHAPS): a resource for assessing exposure to environmental pollutants.* Journal of Exposure Science & Environmental Epidemiology, 2001. **11**(3): p. 231-252.
106. Guarnieri, M. and J.R. Balmes, *Outdoor air pollution and asthma.* The Lancet, 2014. **383**(9928): p. 1581-1592.
107. Nuvolone, D., D. Petri, and F. Voller, *The effects of ozone on human health.* Environmental Science and Pollution Research, 2018. **25**(9): p. 8074-8088.

108. Hubbell, B.J., et al., *Health-related benefits of attaining the 8-hr ozone standard*. Environ Health Perspect, 2005. **113**(1): p. 73-82.

109. Fann, N., et al., *Estimating the National Public Health Burden Associated with Exposure to Ambient PM2.5 and Ozone*. Risk Analysis, 2012. **32**(1): p. 81-95.

110. Bell, M.L., et al., *Ozone and Short-term Mortality in 95 US Urban Communities, 1987-2000*. JAMA, 2004. **292**(19): p. 2372-2378.

111. Ito, K., S.F. De Leon, and M. Lippmann, *Associations between ozone and daily mortality: analysis and meta-analysis*. Epidemiology, 2005. **16**(4): p. 446-57.

112. Levy, J.I., S.M. Chemerynski, and J.A. Sarnat, *Ozone exposure and mortality: an empiric bayes metaregression analysis*. Epidemiology, 2005. **16**(4): p. 458-68.

113. Parodi, S., et al., *Ozone air pollution and daily mortality in Genoa, Italy between 1993 and 1996*. Public Health, 2005. **119**(9): p. 844-50.

114. Turner, M.C., et al., *Long-Term Ozone Exposure and Mortality in a Large Prospective Study*. Am J Respir Crit Care Med, 2016. **193**(10): p. 1134-42.

115. Weschler, C.J., *Ozone's Impact on Public Health: Contributions from Indoor Exposures to Ozone and Products of Ozone-Initiated Chemistry*. Environmental Health Perspectives, 2006. **114**(10): p. 1489-1496.

116. Fiedler, N., et al., *Health Effects of a Mixture of Indoor Air Volatile Organics, Their Ozone Oxidation Products, and Stress*. Environmental Health Perspectives, 2005. **113**(11): p. 1542-1548.

117. Kim, K.-H., S.A. Jahan, and J.-T. Lee, *Exposure to Formaldehyde and Its Potential Human Health Hazards*. Journal of Environmental Science and Health, Part C, 2011. **29**(4): p. 277-299.

118. Salthammer, T., *Acetaldehyde in the indoor environment*. Environmental Science: Atmospheres, 2023. **3**(3): p. 474-493.

119. Chaturvedi, S., et al., *Recent Advancement in Organic Aerosol Understanding: a Review of Their Sources, Formation, and Health Impacts*. Water, Air, & Soil Pollution, 2023. **234**(12): p. 750.

120. Schraufnagel, D.E., *The health effects of ultrafine particles*. Experimental & Molecular Medicine, 2020. **52**(3): p. 311-317.

121. Wolkoff, P., et al., *Acute airway effects of ozone-initiated d-limonene chemistry: Importance of gaseous products*. Toxicology Letters, 2008. **181**(3): p. 171-176.

122. Clausen, P.A., et al., *Chemical and biological evaluation of a reaction mixture of R-(+)-limonene/ozone: Formation of strong airway irritants*. Environment International, 2001. **26**(7): p. 511-522.

123. Sarwar, G. and R. Corsi, *The effects of ozone/limonene reactions on indoor secondary organic aerosols*. Atmospheric Environment, 2007. **41**(5): p. 959-973.

124. Toftum, J. and F. Van Dijken, *Ultra-fine and fine particle formation in a naturally ventilated office as a result of reactions between ozone and scented products*. 2003.

125. Maps, C. 2021; Available from: *https://oehha.ca.gov/calenviroscreen/maps-data*.

126. Xiong, J., et al., *Modeling the Time-Dependent Concentrations of Primary and Secondary Reaction Products of Ozone with Squalene in a University Classroom*. Environmental Science & Technology, 2019. **53**(14): p. 8262-8270.

127. *Air Quality Data (PST) Query Tool*, C.A.R. Board, Editor.

128. Batterman, S., et al., *Ventilation rates in recently constructed U.S. school classrooms*. Indoor Air, 2017. **27**(5): p. 880-890.

129. Aboud, A., et al., *Oxygen gas continuous absorption in the extreme ultraviolet*. Journal of the Optical Society of America, 1955. **45**(9): p. 767-768.

130. Vingarzan, R., *A review of surface ozone background levels and trends.* Atmospheric Environment, 2004. **38**(21): p. 3431-3442.
131. Team, N.A.Q.A.S. *Quantifying Background Ozone*. 2023; Available from: https://aqast.wisc.edu/quantifying-background-ozone.htm.
132. Jaff, D.A., et al., *Scientific assessment of background ozone over the U.S.: Implications for air quality management.* Elementa (Wash D C), 2018. **6**(1): p. 56.
133. EPA, U., *Integrated Science Assessment (ISA) for Ozone and Related Photochemical Oxidants*. 2020.
134. Xiong, R., et al., *A mathematical model for bacterial inactivation.* International Journal of Food Microbiology, 1999. **46**(1): p. 45-55.
135. McMeekin, T., J. Olley, and T. Ross, *Predictive microbiology: theory and application*. 1993: University of Tasmania.
136. Kowalski, W., et al., *Mathematical modeling of ultraviolet germicidal irradiation for air disinfection.* Quantitative microbiology, 2000. **2**(3): p. 249-270.
137. Um, C.Y., et al., *Demonstration of a novel tracer gas method to investigate indoor air mixing and movement.* Indoor Environments, 2025. **2**(1): p. 100081.
138. Gadgil, A.J., et al., *Indoor pollutant mixing time in an isothermal closed room: an investigation using CFD.* Atmospheric Environment, 2003. **37**(39): p. 5577-5586.
139. Drescher, A., et al., *Mixing of a point-source indoor pollutant by forced convection.* Indoor Air, 1995. **5**(3): p. 204-214.
140. Noakes, C., C. Beggs, and P. Sleigh, *Modelling the performance of upper room ultraviolet germicidal irradiation devices in ventilated rooms: comparison of analytical and CFD methods.* Indoor and Built Environment, 2004. **13**(6): p. 477-488.
141. Ratliff, K., *Impact of Test Methods on Far-UVC Performance Against Bioaerosols* 2023: YouTube.
142. CARB, *California Code of Regulations, Regulation for Limiting Ozone Emissions from Air Cleaning Devices, in Title 17, Division 3, Chapter 1, Subchapter 8.7, Article 1*. 2020.
143. UL, *Underwriters Laboratories, Standard 867: Electrostatic Air Cleaners. Northbrook, IL.* 2024.
144. UL, *Underwriters Laboratory, Standard 2998: Environmental Claim Validation Procedure (ECVP) for Zero Ozone Emissions from Air Cleaners. Northbrook, IL.* 2020.
145. ASTM, *Standard Test Method for Chemical Assessment of Air Cleaning Technologies.* 2025.
146. *Revised Standard for UL 867 - Electrostatic Air Cleaners*. 2018.
147. *Illuminate* 2025; Available from: https://illuminate.osluv.org/.
148. Ushio America, I., *Care222® Filtered Far UV-C Excimer Lamp Module – Technical Data Sheet*. 2025.
149. Pistochini, T., et al., *Improving Ventilation and Indoor Environmental Quality in California K-12 Schools.* 2020.
150. Hoang, C.P., K.A. Kinney, and R.L. Corsi, *Ozone removal by green building materials.* Building and Environment, 2009. **44**(8): p. 1627-1633.
151. Lamble, S.P., R.L. Corsi, and G.C. Morrison, *Ozone deposition velocities, reaction probabilities and product yields for green building materials.* Atmospheric Environment, 2011. **45**(38): p. 6965-6972.
152. Lin, C.-C. and S.-C. Hsu, *Deposition velocities and impact of physical properties on ozone removal for building materials.* Atmospheric Environment, 2015. **101**: p. 194-199.
153. Grøntoft, T., J.F. Henriksen, and H.M. Seip, *The humidity dependence of ozone deposition onto a variety of building surfaces.* Atmospheric Environment, 2004. **38**(1): p. 59-68.
154. Pandrangi, L.S. and G.C. Morrison, *Ozone interactions with human hair: Ozone uptake rates and product formation.* Atmospheric Environment, 2008. **42**(20): p. 5079-5089.

155. Tamás, G., et al., *Factors affecting ozone removal rates in a simulated aircraft cabin environment*. Atmospheric Environment, 2006. **40**(32): p. 6122-6133.

156. Fadeyi, M.O., et al., *Impact of Human Presence on Secondary Organic Aerosols Derived from Ozone-Initiated Chemistry in a Simulated Office Environment*. Environmental Science & Technology, 2013. **47**(8): p. 3933-3941.

157. Fischer, A., E. Ljungström, and S. Langer, *Ozone removal by occupants in a classroom*. Atmospheric Environment, 2013. **81**: p. 11-17.

Appendix A: Irradiance Model for GUV Lamp

The theoretical irradiance field calculated using the Link et al. (2023) model was adjusted to represent the irradiance for a USHIO B1 lamp. Data for a Ushio B1 lamp were obtained in IES format from the Illuminate open-source simulation tool website [147]. To represent the B1 lamp output, a dimming correction factor was determined by comparing the irradiance of the B1 lamp to the Link et al. model at a reference position of 1 m from the lamp on-center.

At the on-center position (0° projection angle, r = 1 m), Illuminate reports that irradiance for the USHIO B1 lamp is 12.1 μW/cm^2. This value is consistent with Ushio's specification sheet for the B1 model, which states the lamp has a peak irradiance of 11.2 1 μW/cm^2 at 1 m distance from the lamp [148]. At this same position, the Link model predicts an irradiance of 27.98 μW/cm^2 based on the measured spectral irradiance and geometric projection. The dimming adjustment factor (f_{dim}) was calculated as:

$$f_{dim} = \frac{I_{modeled}}{I_{measured}} = \frac{12.1\ \mu\text{W cm}^{-2}}{27.98\ \mu\text{W cm}^{-2}} = 0.433 \quad \text{(A1)}$$

This factor of 0.43 indicates that Ushio B1 lamp is approximately 43% of the output for the lamp measured and modeled by Link et al. The discrepancy likely reflects differences in the specific lamp and driver tested and/or variations in measurement methodology. One important distinction is that Link et al. measured irradiance up to 0.40 m from the lamp. Thus, irradiance values at 1 m are extrapolated from their fitted relationships, whereas the data reported in Illuminate are direct measurements at 1 m.

To align the spatially detailed Link et al. model with irradiance of the Ushio B1 lamp reported by Illuminate, all irradiance values calculated from the Link model were scaled by this adjustment factor:

$$I_{Adjusted}(r, \theta) = f_{dim} \times I_{Link\ model}(r, \theta) \quad \text{(A2)}$$

Figure 10 illustrates the angular distribution of irradiance as a function of axis projection angle 1 m from the lamp for three cases: (1) values from the USHIO B1 IES file (blue circles), (2) original Link et al. model predictions (orange diamonds), and (3) adjusted Link et al. model values after applying the dimming factor (green crosses). After applying the adjustment, the model predictions (green) closely align with the manufacturer specifications (blue) across the entire angular range from 0° to 55°. This means that the Link et al. model, once adjusted for magnitude, provides a reliable representation of the angular irradiance distribution of the Ushio B1 lamp.

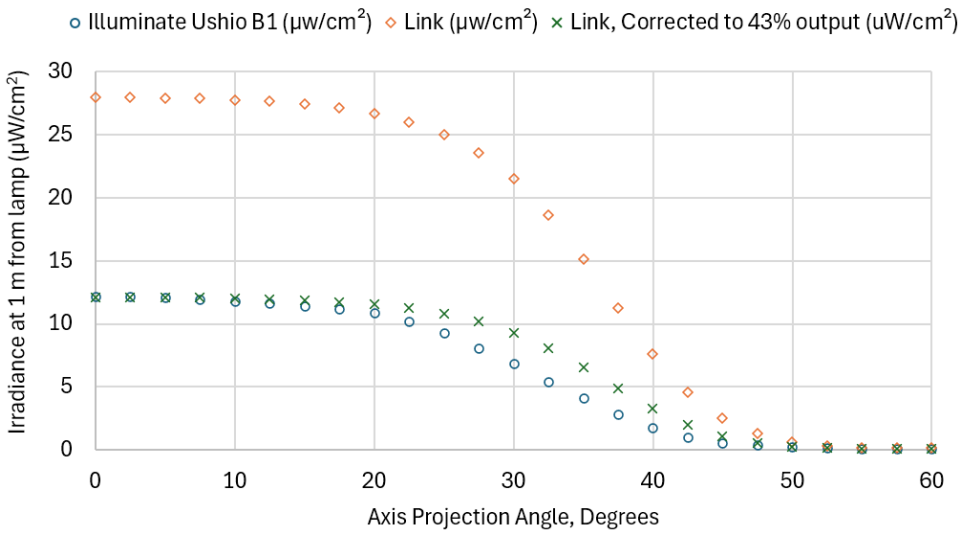

Figure 10. Angular distribution of irradiance at 1 m from the USHIO B1 lamp showing manufacturer specifications (blue), uncorrected Link model predictions (orange), and corrected Link model values after applying the dimming factor of 0.43 (green).

Appendix B: Determination of Ozone Deposition Velocities from Field Data

Deposition velocities for both human skin ($v_{d,h}$) and indoor surfaces ($v_{d,sr}$) were estimated from an independent dataset collected during a 10-day monitoring campaign at a school in Bakersfield, California (October 9–18, 2018). This field study [149], conducted by UC Davis and Lawrence Berkeley National Laboratory, included continuous ozone concentration measurements, which were used to estimate deposition rates under real classroom conditions. The classroom studied had a floor area of 83.31 m^2 (897 ft^2), with dimensions of 11.89 m (39 ft) by 7.01 m (23 ft) and a ceiling height of 2.59 m (8.5 ft). Occupancy during the monitored period averaged 21 individuals, including the teacher. Classroom schedule data were inferred from carbon dioxide (CO_2) measurements, enabling the identification of occupied and unoccupied periods over which deposition velocities were calculated. Concurrent power consumption data for the HVAC system were used to infer time-varying ventilation flow rates. The outdoor air ventilation rate for each of three HVAC operating modes was measured using tracer gas measurement methods: "Vent" (208 $L.s^{-1}$ (442 cfm), lowest power use), "Cool/Heat 1" (297 $L.s^{-1}$ (630 cfm), moderate power), and "Cool/Heat 2" (423 $L.s^{-1}$ (897 cfm), highest power). When the HVAC system was off, an -air change rate of 0.21 h^{-1} was applied, which was equivalent to 12.5 $L.s^{-1}$ for the room volume.

The deposition velocity of ozone to indoor surfaces was estimated using a decay in indoor ozone concentration measured during an unoccupied window on October 12, 2018, from 16:50 to 23:59 (Figure 11b). With no occupancy or mechanical ventilation during this interval, surface deposition was assumed to be the only sink and passive air exchange from outdoors was assumed to be the only source. Equation (1) was applied under these conditions, and model predictions were compared to the observed ozone decay. The optimal deposition velocity was estimated by adjusting its value to minimize the overall difference between modeled and measured concentrations across the times series, quantified using the least-squares norm of the residuals. A pattern search algorithm was used to perform the global optimization. This approach yielded a best-fit deposition velocity of 0.985 m h^{-1}. This value falls within the range reported in prior studies for a variety of indoor surfaces (0.72–2.088 m h^{-1}; [150-153]).

The deposition velocity of ozone to human surfaces was estimated using ozone measurements collected during the occupied portion of October 12, 2018 (Figure 11c). Occupancy was estimated as 1 person when no students were present (as determined by CO_2 data) and 21 people when students were present. The corresponding total human surface area was scaled based on the number of occupants. Although ozone uptake by human surfaces is known to be sensitive to localized airflow near the body [154] and may vary among individuals, the broad occupancy range observed on this day enabled the determination of an average value representative of densely occupied indoor environments. The resulting model predictions and fitted values are presented in Figure 11c. An average deposition velocity of 16.2 m h^{-1} was obtained for ozone removal to occupants, based on an 8-hour window. This value lies within the range reported in the literature for ozone uptake by humans, which spans 7.2 to 22.3 m h^{-1} [74, 155-157].

To evaluate its generality, the derived parameters for deposition to indoor surfaces and humans were applied to other measurement periods not used in the optimization. The model reproduced the observed ozone dynamics well across these additional datasets, lending confidence to both the estimated deposition velocity and the underlying assumptions used in its determination. For a more complete and quantitative comparison, Figure 11d provides scatter plots of the model predictions versus observations for ozone for the 8 test days at the 1 min time resolution of the measured values. Correlation is strong (R^2=0.9), showing that the model explains approximately 90% of observed variability in the classroom with excellent quantitative agreement.

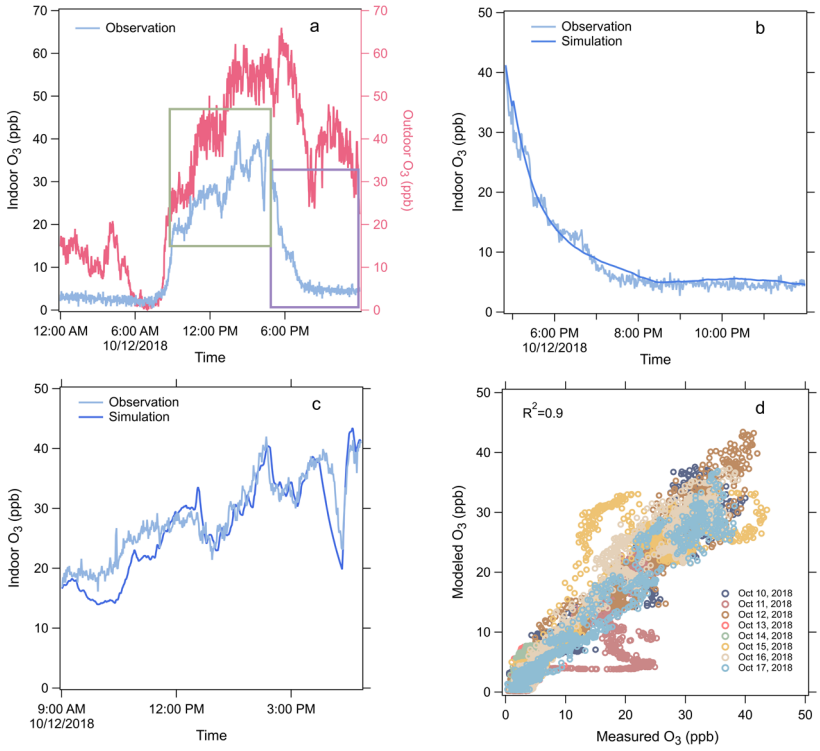

Figure 11. a–c) Comparison between modeled and observed indoor ozone concentrations for October 12, 2018. In panel (a), the green box indicates the occupied time window used to estimate deposition velocity to the human body, while the purple box denotes the unoccupied period used to derive the surface deposition velocity. Panels (b) and (c) show the measured versus predicted time series comparisons for unoccupied and occupied portions used to determine best-fit. (d) Correlation between modeled and measured indoor ozone concentrations for multiple days.